Cell Reports
Medicine

Article

Metabolic profiling of patient-derived organoids reveals nucleotide synthesis as a metabolic vulnerability in malignant rhabdoid tumors

Graphical abstract

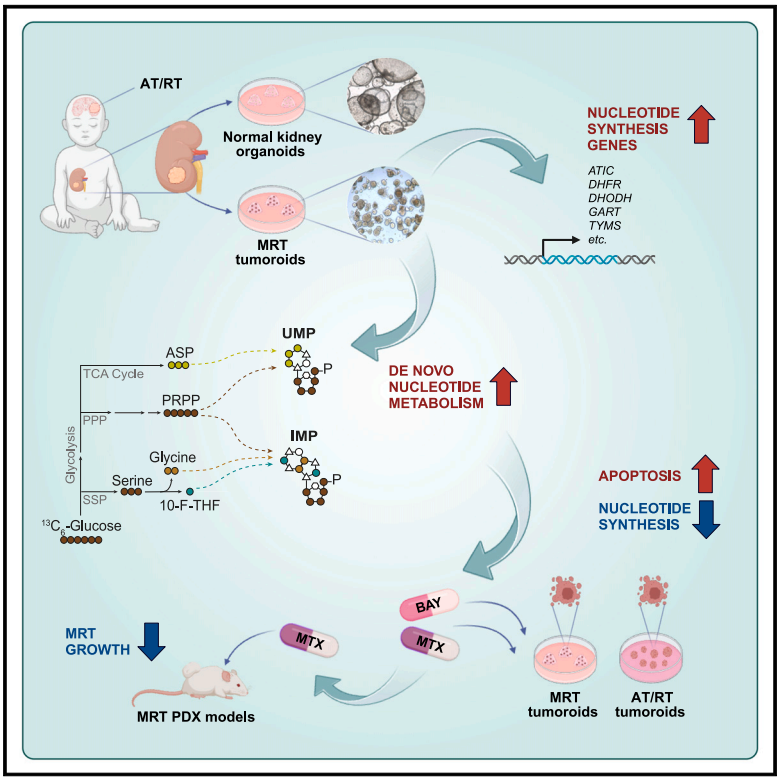

Highlights

- Metabolic fingerprints of pediatric kidney tumors are preserved in tumoroids
- *De novo* nucleotide synthesis is highly activated in MRT and AT/RT
- Nucleotide synthesis inhibition is specifically cytotoxic in MRT and AT/RT
- Nucleotide synthesis inhibition delays MRT growth *in vivo*

Authors

Marjolein M.G. Kes, Francisco Morales-Rodriguez, Esther A. Zaal, ..., Jeroen W.A. Jansen, Celia R. Berkers, Jarno Drost

Correspondence

c.r.berkers@uu.nl (C.R.B.), j.drost@prinsesmaximacentrum.nl (J.D.)

In brief

Malignant rhabdoid tumor (MRT) is an aggressive childhood cancer with limited treatment options. Using patient-derived tumor organoids (tumoroids), Kes et al. identify nucleotide biosynthesis as a vulnerability in MRT. Treatment with methotrexate (MTX) and BAY-2402234 reduced nucleotide levels and induced apoptosis *in vitro*, with MTX demonstrating reduced MRT growth *in vivo*.

Kes et al., 2025, Cell Reports Medicine 6, 101878
January 21, 2025
https://doi.org/10.1016/j.xcrm.2024.101878

CellPress

Cell Reports Medicine

CellPress
OPEN ACCESS

Article

Metabolic profiling of patient-derived organoids reveals nucleotide synthesis as a metabolic vulnerability in malignant rhabdoid tumors

Marjolein M.G. Kes,[1,2,3,6] Francisco Morales-Rodriguez,[1,2,6] Esther A. Zaal,[3,6] Terezinha de Souza,[1,2] Natalie Proost,[4] Marieke van de Ven,[4] Marry M. van den Heuvel-Eibrink,[1,5] Jeroen W.A. Jansen,[3] Celia R. Berkers,[3,*] and Jarno Drost[1,2,7,*]

[1]Princess Máxima Center for Pediatric Oncology, Utrecht, the Netherlands
[2]Oncode Institute, Utrecht, the Netherlands
[3]Division Cell Biology, Metabolism & Cancer, Department Biomolecular Health Sciences, Faculty of Veterinary Medicine, Utrecht University, Utrecht, the Netherlands
[4]Preclinical Intervention Unit of the Mouse Clinic for Cancer and Ageing (MCCA), Netherlands Cancer Institute, Amsterdam, the Netherlands
[5]Division of Child Health, Wilhelmina Children's Hospital, Utrecht University, Utrecht, the Netherlands
[6]These authors contributed equally
[7]Lead contact
*Correspondence: c.r.berkers@uu.nl (C.R.B.), j.drost@prinsesmaximacentrum.nl (J.D.)
https://doi.org/10.1016/j.xcrm.2024.101878

SUMMARY

Malignant rhabdoid tumor (MRT) is one of the most aggressive childhood cancers for which no effective treatment options are available. Reprogramming of cellular metabolism is an important hallmark of cancer, with various metabolism-based drugs being approved as a cancer treatment. In this study, we use patient-derived tumor organoids (tumoroids) to map the metabolic landscape of several pediatric cancers. Combining gene expression analyses and metabolite profiling using mass spectrometry, we find nucleotide biosynthesis to be a particular vulnerability of MRT. Treatment of MRT tumoroids with *de novo* nucleotide synthesis inhibitors methotrexate (MTX) and BAY-2402234 lowers nucleotide levels in MRT tumoroids and induces apoptosis. Lastly, we demonstrate *in vivo* efficacy of MTX in MRT patient-derived xenograft (PDX) mouse models. Our study reveals nucleotide biosynthesis as an MRT-specific metabolic vulnerability, which can ultimately lead to better treatment options for children suffering from this lethal pediatric malignancy.

INTRODUCTION

Kidney cancer is the second most common solid cancer in children. Pediatric kidney tumors mostly encompass Wilms tumors, representing ~80% of cases, but also renal cell carcinomas (RCCs), clear cell sarcomas, and malignant rhabdoid tumors (extracranial MRT [ecMRT]) can occur.[1] Malignant rhabdoid tumors (MRTs) are particularly aggressive malignancies that are typically diagnosed in young children, mostly infants, and can develop throughout the body, including in the brain, where they are called atypical teratoid/rhabdoid tumors (AT/RTs).[2–4] Based on DNA methylation patterns and transcriptome profiles, AT/RT can be further subdivided into three subgroups called MYC, Sonic hedgehog (SHH), and Tyrosinase (TYR).[5–7] MRT arises as a consequence of derailed differentiation and lineage specification during fetal development,[8–11] which is caused by the biallelic inactivation of *SMARCB1* (~95% of cases) or *SMARCA4* (~5% of cases), both of which are subunits of the SWItch/Sucrose Non-Fermentable (SWI/SNF) chromatin-remodeling complex.[12–14] To date, patient survival is dependent on intensive therapeutic approaches, including chemotherapy, radiotherapy, and surgical intervention. However, in patients that are younger and/or present with metastatic disease, the survival rates remain exceedingly low, highlighting the urgent need for therapeutic innovation.

Metabolic rewiring is considered a hallmark of cancer,[15] indispensable for tumor cells to maintain their proliferative capacity. As such, metabolic inhibitors have a long history of success in cancer treatment, with compounds targeting metabolic enzymes being in various stages of drug development.[16–18] Metabolic reprogramming is also profound in adult clear cell RCC,[19–21] where vast changes in glucose, lipid, and amino acid metabolism are often observed.[22] These broad changes in cellular metabolism result from genetic mutations in important metabolic regulators. Notable examples include mutations in the von Hippel-Lindau (VHL) gene,[23] resulting in accumulation of hypoxia-inducible factor 2α (HIF-2α),[22] and the PI3K/AKT/mTOR axis, a major regulator of cellular metabolism that is modestly mutated yet aberrantly activated in adult RCC[24,25] as well as in many other cancer types.[26,27] Importantly, the first generation of mTORC1 inhibitors was first approved for use in advanced RCC,[28] underscoring that intervening in metabolic processes can lead to opportunities in clinical practice. Also, a recent study in AT/RT[29] revealed that targeting metabolic vulnerabilities in synergy with standard-of-care therapeutics was able to improve therapeutic outcomes, highlighting the potential of metabolic therapy in rhabdoid

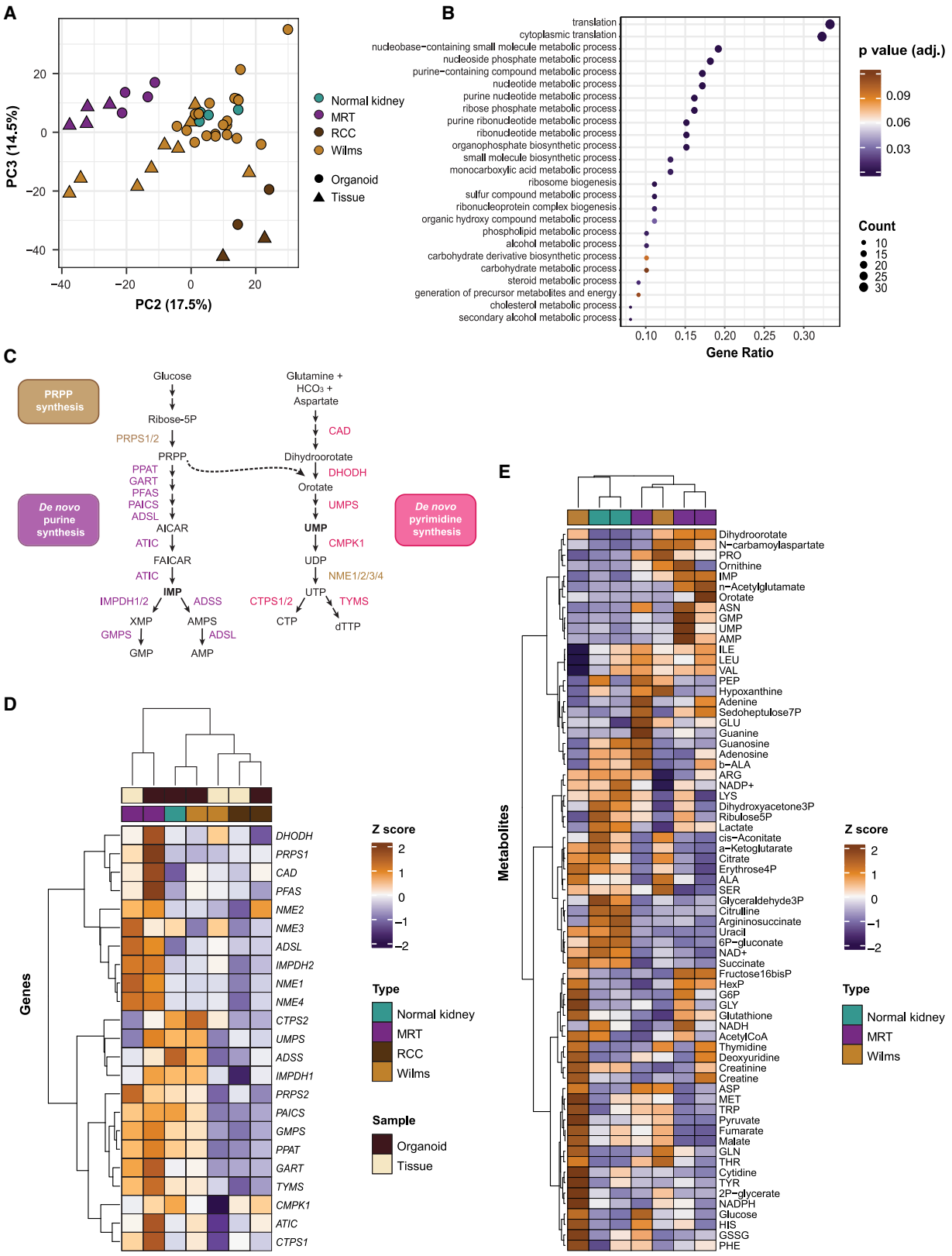

(legend on next page)

tumors. However, the metabolic vulnerabilities of pediatric kidney cancers, and in particular the metabolic rewiring undergone by MRT, so far remain largely unexplored.

Recapitulating many features of the tissues they were derived from, organoids represent a more relevant *in vitro* model system to study tissue homeostasis and disease than the classical 2D-grown (cancer) cell models.[30] While maintaining the genetic and phenotypic heterogeneity to a large extent, tumor-derived organoids (tumoroids) typically do not capture the tumor microenvironment. Organoids therefore represent a reductionist model allowing for the study of tumor-intrinsic vulnerabilities.[31] Originally established for a wide range of different adult cancers,[32–36] organoid technology has now also been successfully applied to several pediatric cancers, including pediatric kidney tumors.[37–41]

Here, we use tumoroids to profile the metabolism of several pediatric kidney cancers. By combining gene expression analyses on patient tissues and tumoroids, and metabolite profiling on tumoroids using mass spectrometry, we find that nucleotide biosynthesis is a particular vulnerability of MRT that should be therapeutically explored.

RESULTS

Pediatric kidney tumor subtypes have distinct metabolic fingerprints that are maintained in tumoroids

We started our investigation into the metabolic signatures of pediatric kidney tumors by analyzing a bulk mRNA sequencing gene expression dataset of tumoroids and matching tumor tissues of the three main kidney cancer subtypes (Wilms tumor, RCC, and MRT of the kidney), as well as normal kidney-derived organoids.[38] Principal-component (PC) analysis focusing on metabolic genes specifically (Table S1) showed that tumoroids and tumor tissues clustered based on histopathological entity (Figure 1A), indicating that tumor entity-specific metabolic profiles are largely retained in tumoroids, at least at the gene expression level. While Wilms tumors displayed a more heterogeneous metabolic gene expression pattern, MRT tissues and tumoroids derived thereof represented a distinct cluster separate from the other renal tumor entities and normal kidney organoids (Figure 1A).

To identify which metabolic pathways are responsible for the MRT-specific expression profile, we performed Gene Ontology (GO) term enrichment analysis on the top 100 MRT-specific metabolic genes (Figure 1B; Table S2). MRT tissues and tumoroids displayed a significant enrichment of genes involved in purine and pyrimidine nucleotide biosynthesis (Figure 1B). Using unsupervised hierarchical clustering based on mRNA expression of *de novo* nucleotide biosynthesis genes, we observed tumor-specific clustering with the highest expression in MRT (Figure 1C and 1D). Wilms tumors, on the other hand, displayed a significant increase in genes involved in (glycero)phospholipid metabolism (Figures S1A and S1B), underscoring that different pediatric kidney tumor subtypes display unique metabolic traits. These associations were corroborated using an independent gene expression dataset of pediatric renal tumor tissues, derived from the TARGET database[42](Figures S1C–S1F).

To verify that the identified metabolic gene signatures also result in differential metabolite levels, we performed liquid chromatography-mass spectrometry (LC-MS)-based metabolomics in MRT and Wilms tumoroids as well as in normal kidney tissue-derived organoids (Figure 1E). Unsupervised hierarchical clustering of the metabolites detected across all samples shows distinct metabolic profiles in MRT and Wilms tumoroids as compared to normal kidney organoids. Moreover, levels of metabolites involved in both pyrimidine and purine biosynthesis were highest in MRT tumoroids (dihydroorotate, N-carbamoyl-aspartate, uridine monophosphate [UMP] and inosine monophosphate [IMP], guanine monophosphate [GMP], and adenosine monophosphate [AMP]) (Figure 1E). These elevated purine and pyrimidine metabolite levels in MRT tumoroids, relative to normal kidney organoids, were confirmed and further characterized in subsequent studies (Figure S1G). Wilms tumoroids, on the other hand, displayed high levels of tricarboxylic acid (TCA)-cycle metabolites. Together, these data show that pediatric kidney tumor subtypes have distinct metabolic profiles based on gene expression and metabolite levels, with MRT showing increased nucleotide biosynthesis.

Inhibition of *de novo* nucleotide synthesis is a vulnerability of MRT

To investigate whether the observed increase in nucleotide metabolism in MRT represents a putative therapeutic vulnerability in ecMRT specifically or in rhabdoid tumors in general, we set out to inhibit these pathways pharmacologically in a range of rhabdoid and non-rhabdoid tumoroids. Methotrexate (MTX)

Figure 1. Pediatric kidney tumor subtypes have different metabolic fingerprints

(A) Unsupervised principal-component (PC) analysis of gene expression profiles for metabolic genes (n = 2,076 genes) present across all n = 45 samples (n = 30 organoid samples and n = 15 matching patient tissue samples), showing the difference between normal kidney (n = 4, blue), MRT (n = 8, purple), RCC (n = 4, dark brown), and Wilms tumor samples (n = 29, brown). Organoid/tumoroid samples are represented by dots, and matching tissue samples are depicted as triangles.

(B) Gene Ontology (GO) term enrichment analysis of the top 100 MRT-specifying, differentially expressed metabolic genes (DEGs). Image shows the top 25 significantly enriched biological processes according to gene ratio, i.e., the percentage of DEGs within a given GO term.

(C) Schematic and simplified representation of the purine and pyrimidine monophosphate biosynthesis pathways. The main nucleotide monophosphate precursors are written in bold. Colors indicate purine biosynthesis enzymes (purple), pyrimidine biosynthesis enzymes (pink), and enzymes shared between the pathways (brown).

(D) Z score-based heatmap visualizing the average expression of genes involved in the purine and pyrimidine ribonucleoside monophosphate biosynthesis pathways for each kidney sample type group. All n = 8 MRT (n = 4 organoid; n = 4 tissue sample), n = 4 RCC (n = 2 organoid; n = 2 tissue samples), n = 29 Wilms tumor (n = 20 organoid; n = 9 tissue samples), and n = 4 normal kidney (n = 4 organoid samples) samples were included for this analysis.

(E) Z score-based heatmap representing hierarchical clustering of the metabolites detected across all indicated organoid/tumoroid cultures in a 24-h steady-state metabolomics study. In total, n = 7 models (n = 2 Wilms tumor; n = 2 normal kidney; n = 3 MRT) were used that were representative for each kidney organoid subtype.

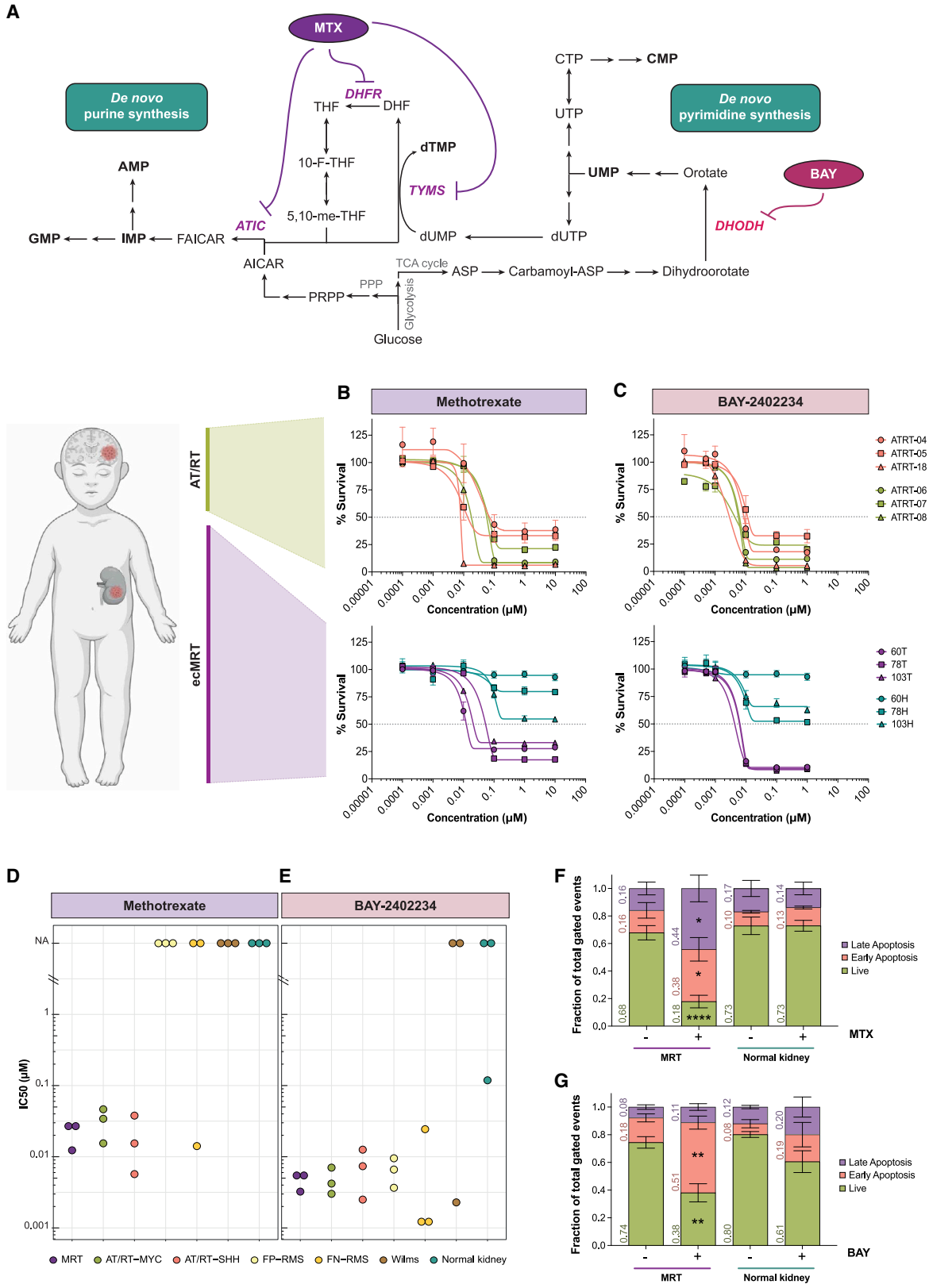

(legend on next page)

interferes with purine nucleotide and thymidylate synthesis via multiple mechanisms (Figure 2A) and is widely used in the clinic to treat different cancer types.[43–47] BAY-2402234 (BAY, Orludodstat) is a potent inhibitor of the *de novo* pyrimidine synthesis enzyme DHODH[48,49] (Figure 2A). Recently, BAY has shown promising preclinical results in various (pediatric) brain tumors.[48–51] Hence, we treated three MRT and six AT/RT rhabdoid tumoroid models (three AT/RT-SHH and three AT/RT-MYC[41]) with different concentrations of MTX and BAY. Normal kidney organoids as well as tumoroids derived from other tumor entities, such as rhabdomyosarcoma (RMS)[40] and Wilms tumors, were also included. A detailed overview describing the clinical characteristics of the patient-derived tumoroid models can be found in Table S3. All tested MRT and AT/RT tumoroids were significantly more sensitive to MTX treatment compared to normal kidney organoids (Figure 2B), RMS, and Wilms tumoroids (Figure 2D and Figures S2A, S2B, and S2E). Whereas the average IC_{50} value of MTX in rhabdoid tumoroids was 24.6 nM (±13.4), the majority of normal kidney, RMS, and Wilms tumor organoids did not reach 50% inhibition by MTX (Figure 2D). A more heterogeneous response was observed upon BAY treatment with MRT, AT/RT, and RMS consistently showing very high sensitivity with IC_{50} values within the nanomolar range (average IC_{50} values: 4.7 nM [±1.4], 6.1 nM [±3.8], and 7.8 nM [±8.8], respectively), while normal kidney organoids and Wilms tumoroids displayed a lower and more variable sensitivity (Figure 2C and 2E and S2C–S2E). Next, we performed Annexin V/DAPI labeling on MRT tumoroids and normal kidney organoids to determine whether the observed inhibitory effects were cytotoxic or cytostatic. We found that treatment of normal kidney organoids did not induce any significant apoptosis. In contrast, a significant increase in early and late apoptotic cells could be observed in MRT tumoroids upon treatment with either MTX (2.7-fold [±0.56] change) or BAY (2.5-fold [±0.40] change) (Figures 2F, 2G, S2F, and S2G). Summarizing, our results show that targeting nucleotide metabolism marks a therapeutic vulnerability in MRTs.

MTX and BAY inhibit *de novo* nucleotide biosynthesis in MRT

To further analyze nucleotide metabolism in MRT, we optimized previously established isotope tracer workflows[52,53] in our normal kidney organoid and tumoroid models. MRT tumoroids and normal kidney organoids were grown in the presence of [U-$^{13}C_6$]-glucose, after which the incorporation of ^{13}C carbons in nucleotides over time was monitored using LC-MS. Our results show that MRT primarily utilize glucose to produce metabolites involved in glycolysis, the TCA cycle, the pentose phosphate pathway (PPP), oxidative processes, and nucleotide biosynthesis pathways. Additionally, a substantial incorporation of labeled glucose was detected in the methylation-related metabolites S-adenosyl-homocysteine and S-adenosyl-methionine and amino acids alanine, aspartate (ASP), glutamate, and serine, the majority of which play key roles in *de novo* nucleotide synthesis. As expected, the nine essential amino acids (HIS, ILE, LEU, LYS, MET, PHE, THR, TRP, and VAL), which cannot be endogenously synthesized by human cells, remained unlabeled (Figure S3A).

Focusing on nucleotide production, glucose-derived carbons contribute to both purines (e.g., IMP) and pyrimidines (e.g., UMP) via several routes (Figure 3A), whereby *de novo* synthesis and salvage pathways result in different isotopologues. The PPP generates ribose-5-phosphate, thereby providing the pentose sugar ([M+5]) for both purines and pyrimidines. The serine synthesis pathway (SSP) provides glycine ([M+2]) and 10-formyl-tetrahydrofolate (10-F-THF, [M+1]), which are incorporated in the purine nucleobase, while aspartate ([M+3]), which is produced via the TCA cycle, contributes carbons to pyrimidine nucleobases. Thus, *de novo* synthesis of purines and pyrimidines can result in isotopologues with 1–9 labeled carbons ([M+1–9]), whereas solely the ribose moiety is labeled during nucleotide salvage, resulting in [M+5] isotopologues only. Total nucleotide levels were higher in MRT compared to normal kidney organoids, as exemplified by ADP (purine) and UDP (pyrimidine) (Figure 3B). In addition, while in normal kidney organoids only ADP and UDP [M+0] and [M+5] were present, MRT tumoroids displayed amplified levels of ADP and UDP [M+6–8], indicating increased *de novo* synthesis of nucleotides (Figure 3B). Similar labeling patterns were observed for the nucleotide monophosphates, the end products of the nucleotide biosynthetic pathways. However, due to lower overall levels of nucleotide monophosphates in normal kidney organoids, which hindered the detection and visualization of all isotopologues, we here show the nucleotide diphosphates. Investigating the fraction of ^{13}C labeling in nucleotides over time, MRT showed a significantly faster production of [M+5] ADP and UDP (i.e., labeling of the ribose moiety), reaching a plateau at the same level as normal kidney organoids after 24 h (Figure 3C). Moreover, the combined fraction of isotopologues higher than [M+5] increased over time in MRT tumoroids but was absent in normal kidney organoids. These findings were recapitulated in AT/RT tumoroids, in which [U-$^{13}C_6$]-glucose-derived carbons were incorporated into ADP and UDP at rates comparable to MRT and ADP and UDP [M+>5] were also produced (Figures S3B–S3D). Together, these findings indicate that MRT and AT/RT tumoroid models show

Figure 2. *De novo* nucleotide synthesis is a metabolic vulnerability of rhabdoid tumors

(A) Schematic overview of the mechanisms of action of methotrexate (MTX) and BAY-2402234 (BAY). MTX targets *de novo* purine synthesis and thymidylate synthesis via inhibition of the enzymes dihydrofolate reductase (DHFR), 5-aminoimidazole-4-carboxamide ribonucleotide formyltransferase/IMP cyclohydrolase (ATIC), and thymidylate synthase (TYMS). BAY targets *de novo* pyrimidine synthesis via inhibition of the dihydroorotate dehydrogenase (DHODH) enzyme.

(B and C) Dose-response curves of MTX (B) and BAY (C) for the indicated organoid and tumoroid cultures. Clinical characteristics of our patient-derived models can be found in Table S3. Data points are represented as the mean ± SD of three independent experiments, each consisting of quadruplicate measurements. Data are normalized to DMSO vehicle (100%). The gray dashed horizontal line represents a viability of 50% (IC_{50}).

(D and E) Scatterplots showing individual IC_{50} values of MTX (D) and BAY (E) for different tumoroid and organoid models, grouped per histopathological entity.

(F and G) Bar graphs representing live (green), early apoptotic (pink), and late apoptotic (purple) cell fractions of MRT and normal kidney organoids upon treatment with 400 nM MTX (F) or 50 nM BAY (G) for 120 h. The means ± SEM of $n = 3$ kidney organoid models are plotted. p values were generated by performing multiple paired Student's t test (*, $p < 0.05$; **, $p < 0.01$; ****, $p < 0.0001$).

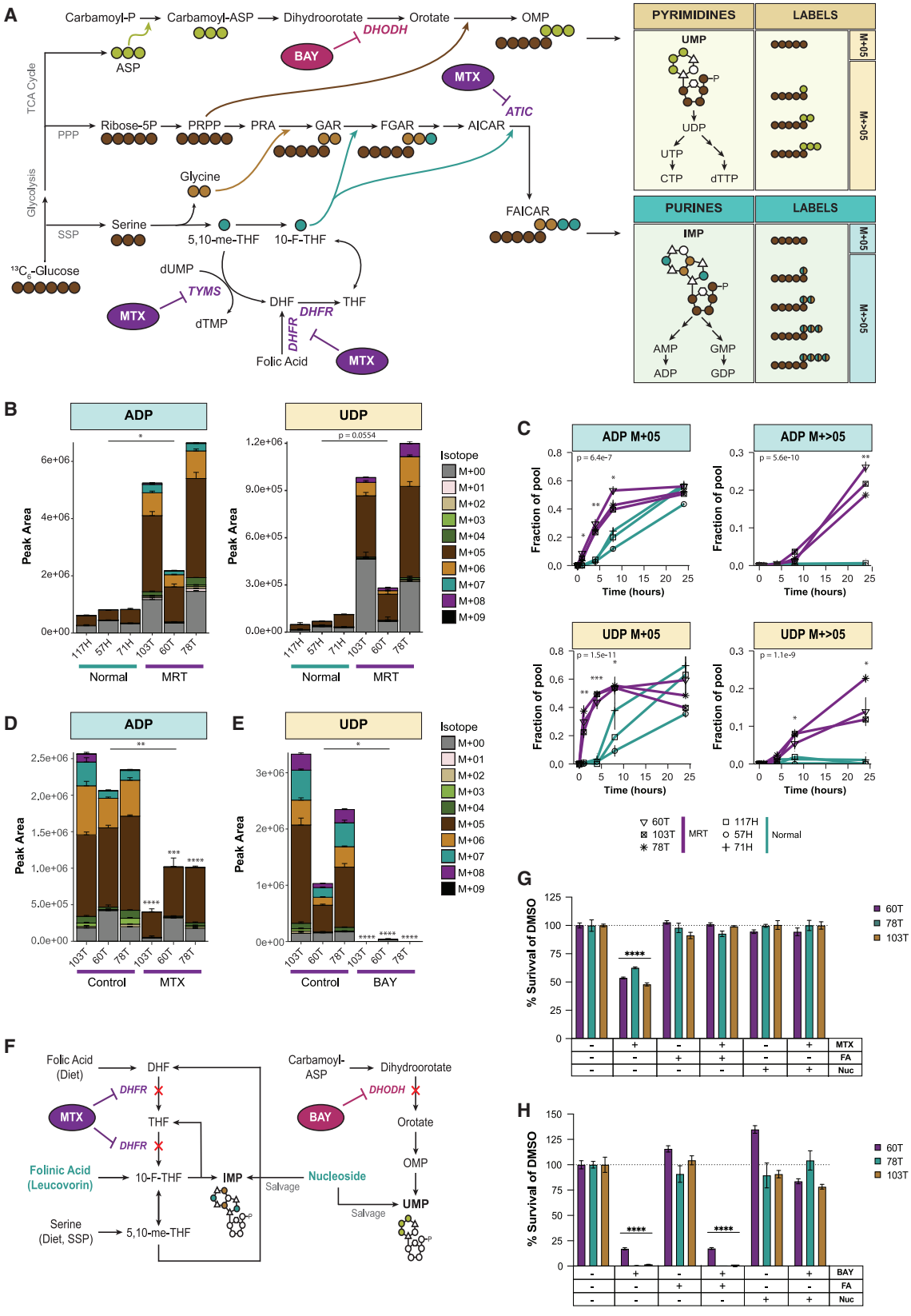

(legend on next page)

increased *de novo* nucleotide biosynthesis as compared to normal kidney organoids.

MTX is known to inhibit the *de novo* purine synthesis by acting on dihydrofolate reductase (DHFR), which is involved in one-carbon/folate metabolism. BAY, on the other hand, is a specific inhibitor of DHODH, an enzyme involved in the *de novo* pyrimidine synthesis (Figures 2A and 3A). To examine the impact of MTX and BAY on glucose-dependent metabolic pathways, particularly *de novo* nucleotide synthesis, we performed [U-$^{13}C_6$]-glucose tracing in MRT organoids in the presence and absence of MTX or BAY. Focusing on metabolites exhibiting $\geq$40% glucose incorporation after 24 h of labeling, as identified in Figure S3A, treatment with BAY (Figure S3F) had broader effects on [U-$^{13}C_6$]-glucose incorporation into glucose-dependent metabolites than MTX (Figure S3E), with the effects primarily being inhibitory. The most pronounced alterations were observed in the nucleotide biosynthesis pathways, amino acids, and the TCA cycle, with minimal to no changes detected for glycolytic metabolites (Figures S3E and S3F). While the MTX-induced changes in fractional incorporation of glucose were smaller, the most substantial changes were observed in metabolites related to nucleotide synthesis pathways (Figure S3E). In addition to reducing glucose incorporation into nucleotides, MTX also decreased the total levels of purines, in particular the [M>+5] fractions (Figure 3D). After BAY treatment, a marked decrease in levels of all UDP isotopologues was observed, indicating that pyrimidine synthesis is inhibited (Figure 3E). As expected, BAY treatment also resulted in accumulation of metabolites upstream of DHODH, such as aspartate and carbamoyl-aspartate, and lower levels of its downstream metabolite orotate (Figure S3G).

To confirm the metabolic impact of MTX and BAY on the transcriptional level, we set out to investigate the effects of these drugs on the expression of pivotal enzymes in the *de novo* nucleotide synthesis pathway. Hence, we performed mRNA bulk sequencing on patient-matched MRT tumoroids and normal kidney organoids exposed to DMSO, MTX, or BAY. In line with our previous results (Figure 1D), MRT displayed higher expression levels of *de novo* nucleotide biosynthesis genes compared to normal kidney organoids (Figure S3H). Treatment with MTX and BAY induced a downregulation of the majority of nucleotide biosynthesis genes in MRT specifically (Figures S3I and S3J). Notably, BAY treatment effectively restored the expression levels of its direct target DHODH in MRT to those comparable to normal kidney organoids at baseline (Figure S3K). These results validate the metabolic effects of MTX and BAY at the transcriptional level and indicate that the MRT-specific sensitivity to nucleotide biosynthesis inhibition is, at least in part, attributable to the higher baseline expression of key enzymes in MRT tumoroids compared to normal kidney organoids.

To further confirm that the observed cytotoxicity of MTX and BAY on MRT is caused by on-target effects of the drugs, we performed rescue experiments by supplementing folinic acid (FA) or nucleosides during drug treatment (Figure 3F). Both FA and nucleosides completely rescued the MTX-induced cell death (Figure 3G), while only nucleoside supplementation rescued BAY-induced cell death (Figure 3H), which is in line with the proposed mechanisms of action of both drugs on the nucleoside biosynthesis pathways. Together, these results verify that MTX and BAY induce cell death in MRT via inhibition of *de novo* nucleotide synthesis.

MTX inhibits *in vivo* MRT growth

Since MTX is already broadly used in the clinic as an anti-cancer therapy, we next aimed to investigate whether MTX can inhibit MRT growth *in vivo*. To prevent folic acid, which is normally present in high levels in mouse chow, from abrogating the efficacy of MTX,[54] all mice were put on a folic acid-depleted diet during treatment. To this end, immunodeficient non-obese diabetic (NOD)-severe combined immunodeficiency (SCID) IL2Rgnull mice were subcutaneously injected with MRT tumoroids, giving rise to tumors that histologically resembled primary MRT tissue (Figure S4A). When tumor volumes reached 100–150 mm^3, mice were transitioned to a folic acid-depleted diet. After one week on the diet, mice were subjected to daily intraperitoneal (i.p.) injections of 0.75 mg/kg MTX, established by prior maximum tolerated dose studies or vehicle (saline) for a duration of four weeks (Figure 4A).

The 78T MRT model showed accelerated *in vivo* growth (Figures 4C, 4E, 4G, S4C, and S4D) compared to the 103T MRT model (Figures 4B, 4D, 4F, and S4B). Based on the differences

Figure 3. MTX and BAY target MRT via inhibition of *de novo* nucleotide biosynthesis

(A) Schematic overview of the incorporation of carbons from [U-$^{13}C_6$]-glucose into purines and pyrimidines. The ribose ring is produced via the pentose phosphate pathway (PPP; brown), resulting in UMP [M+5] and IMP [M+5]. The serine synthesis pathway (SSP) provides carbons for the purine nucleobase via glycine (light brown, [M+2]) or one-carbon metabolism (blue; [M+1]). Combinations of these pathways result in various purine labeling patterns. Aspartate (ASP) is providing carbons for the pyrimidine nucleobase (green; [M+3]), giving rise to the various pyrimidine labeling patterns. Circles represent carbon; triangles represent nitrogen.

(B) Isotope distribution of ADP and UDP in three normal kidney organoids and three MRT tumoroids after 24 h of culturing in [U-$^{13}C_6$]-glucose. Student's t test between normal and MRT was performed on mean peak area of the sum of all isotopologues of individual cell lines.

(C) Incorporation of glucose-derived ^{13}C in ADP and UDP over time in three normal kidney organoids (blue) and three MRT tumoroids (purple) after 24 h of culturing in [U-$^{13}C_6$]-glucose. The effect of organoid type (normal kidney or MRT) on glucose incorporation over time was analyzed using a linear model with an interaction term of class and time. Significant interaction between class and time was defined as an improved model fit with interaction term of class and time over a model lacking this interaction. Student's t tests were performed on individual time points.

(D and E) Isotope distribution of ADP and UDP in three MRT tumoroids after 24 h of culturing in [U-$^{13}C_6$]-glucose in the presence and absence of 400 nM MTX (D) or 5 nM BAY (E). Student's t test between normal and MRT organoids was performed on mean peak area of the sum of all isotopologues of individual cell lines.

(F) Graphical representation of the mechanism by which folinic acid and nucleosides (blue fonts) rescue the effects of MTX and BAY.

(G and H) Bar graph showing the viability of three MRT organoid lines after 120 h of treatment with 400 nM MTX (G) or 50 nM BAY (H), alone and in combination with either nucleosides or folinic acid. Bars show the mean ± SEM of four technical replicates. Results were normalized to DMSO-treated control cells (100%) for each separate MRT line. (*, $p < 0.05$; **, $p < 0.01$; ***, $p < 0.001$; ****, $p < 0.0001$).

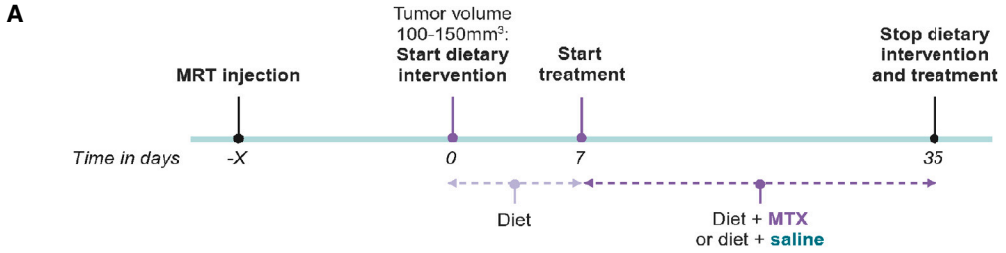

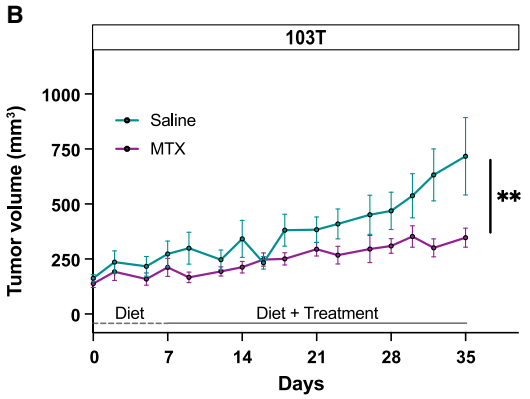

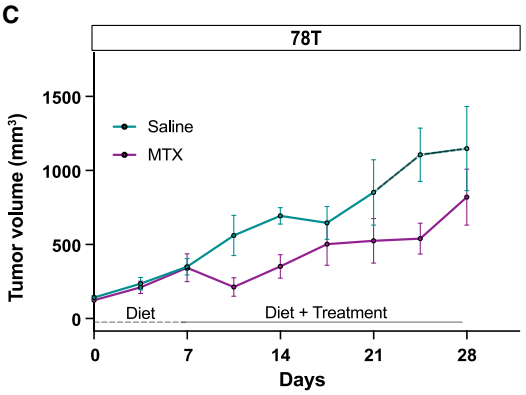

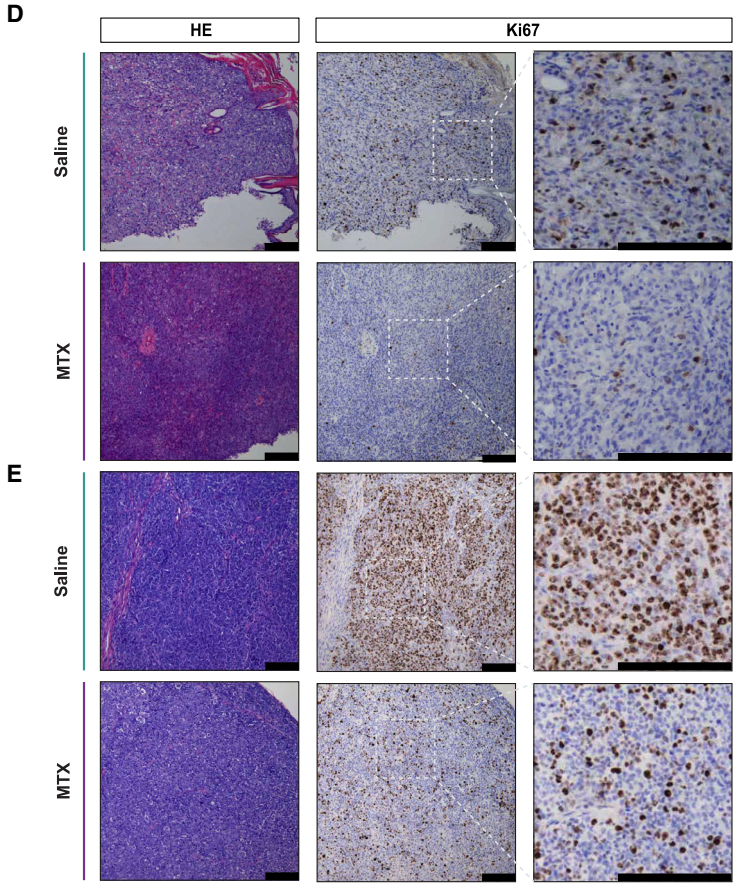

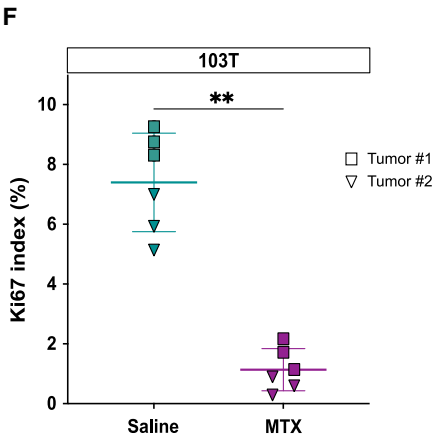

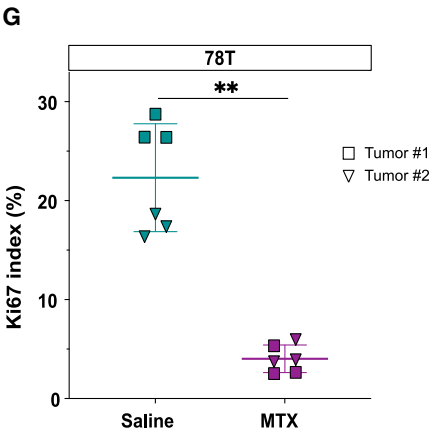

(legend on next page)

in growth dynamics between the two PDX models, mice were treated with MTX for either 21 (78T) or 28 days (103T).

In line with our *in vitro* observations, MTX treatment resulted in a delayed growth and decreased proliferation of MRT tumors compared to the saline-treated mice (Figures 4B–4G and S4B–S4D). However, body weight measurements did show signs of MTX-related toxicity, showing >20% weight loss in some MTX-treated mice (Figure S4E). Despite associated toxicity, daily treatment with MTX effectively delayed the growth and reduced the proliferation of MRT *in vivo*, consistent with our *in vitro* observations.

DISCUSSION

To accommodate their high energy demand and sustain growth, tumors must rewire their metabolism. As such, metabolic rewiring is considered one of the hallmarks of cancer,[15] which can potentially provide an "Achilles heel" of tumors that can be therapeutically exploited. We here investigated the metabolic signatures of MRT, an aggressive childhood malignancy with dismal prognosis,[55] using MRT tumor organoids (tumoroids). Such patient-derived tumoroid models have emerged as robust preclinical models for cancer research,[31] recapitulating several features of the tissues they were derived from, such as genetic, transcriptomic, and phenotypic features.[38] To which extent the metabolic profiles of tumoroids also match those of the primary tissues was so far unclear. We here demonstrate that pediatric kidney tumoroids largely retain the metabolic profiles of the tumors they were derived from, with high expression of enzymes involved in nucleotide biosynthesis and (glycero)phospholipid metabolism in MRT and Wilms tumors, respectively. Notably, mapping the metabolome of our patient-derived tumoroid models revealed patient-specific metabolic signatures, demonstrating that interpatient heterogeneity is captured by our patient-derived tumoroids, which we consider a valuable strength of our *in vitro* 3D models. Despite the patient-specific heterogeneity, nucleotide metabolism consistently emerged as a metabolic dependency across our MRT models. We therefore reasoned that the observed increase in nucleotide biosynthesis in MRT could present a therapeutic opportunity. Indeed, we demonstrate that ecMRT as well as their intracranial counterpart AT/RT are particularly sensitive to the anti-folate drug MTX and DHODH inhibitor BAY, in contrast to normal kidney organoids. All MRT tumoroid models were highly responsive to treatment with MTX and BAY, with IC_{50} values in the nanomolar range. Validation of our findings in two independent MRT PDX models demonstrated that treatment utilizing MTX delayed tumor growth *in vivo*. Given the observed tumor progression under treatment and the highly aggressive nature of MRT, MTX monotherapy will likely not be sufficient for effective clinical application. Incorporation of MTX into the current standard-of-care treatment for MRT patients, however, could potentially enhance patient survival rates. Since intrathecal administration of MTX is already part of the standard treatment protocol for AT/RT patients,[56] this approach appears feasible. As the combined use of MTX and BAY did not demonstrate any synergistic or additive effects *in vitro* (data not shown), further evaluation of this combination therapy was not pursued.

Nucleotide synthesis inhibitors are clinically tolerated with a manageable toxicity profile. The history of MTX dates to 1948, when the anti-folate aminopterin was successfully used for the treatment of childhood acute lymphoblastic leukemia (ALL).[57] In current treatment protocols, the related agent MTX is part of the treatment regimen of many adult[58] as well as childhood cancers, including pediatric ALL,[43] non-Hodgkin's lymphoma,[59] osteosarcoma,[60–62] and various brain tumors,[63–66] including AT/RT.[67] Although the therapeutic value of MTX is clear, its use can be associated with a variety of adverse effects, with more frequent and more severe side effects being observed with increased dose or dosing frequency.[68] Therefore, patients treated with MTX receive close monitoring of their health and, if necessary, dose changes and/or leucovorin (FA) rescue therapy.[56,58] Also in our *in vivo* experiments, daily administration of MTX led to significant weight loss/toxicity in two of the fourteen treated mice, underscoring the potential harmful effects of long-term, frequent dosing as well as the importance of close monitoring when administering this therapy to patients.

Our study also suggests that BAY provides a therapeutic opportunity for the treatment of children with rhabdoid tumors, which merits further evaluation. Given the different mode of action of BAY compared to MTX and the observed effects in our tumoroid models, BAY may provide a better tolerable alternative to MTX for the treatment of ecMRT and AT/RT. Recent literature has shown that monotherapy with BAY results in increased survival rates in mice bearing (pediatric) brain tumor xenografts.[48–51] Notably, a recent clinical trial investigating advanced myeloid malignancies (NCT03404726) found that daily oral administration of BAY was safe. The demonstrated efficacy in animal models and the previously established safety profiles of BAY in both animal models and human clinical trials suggest significant potential for the commencement of clinical trials using BAY.

Consistent with our findings, several studies propose that gemcitabine, a pyrimidine nucleoside analog, stands out as one of the few effective chemotherapeutic options to manage

Figure 4. Methotrexate demonstrates *in vivo* efficacy in MRT xenograft models

(A) Experimental overview of *in vivo* MTX testing. Mice were subcutaneously injected with MRT organoids. When tumor volumes reached 100–150 mm^3, mice were subjected to a folic acid-depleted diet. After one week on the diet, mice received daily intraperitoneal (i.p.) injections of 0.75 mg/kg MTX or saline vehicle for a duration of four weeks.

(B and C) Tumor growth of MRT models 103T ($n = 9$ mice per treatment arm, B) and 78T ($n = 5$ mice per treatment arm, C) in mice treated with either saline vehicle (blue) or 0.75 mg/kg MTX (purple). The dotted blue line from days 21–28 in the saline group (C) indicates the period during which $n = 1$ mouse reached a tumor volume >1,500 mm^3. Data are represented as means ± SEM. p value was calculated using a two-tailed unpaired Student's t test (**, $p < 0.01$).

(D and E) Hematoxylin & Eosin (HE) and Ki67 staining on saline vehicle-treated (top) and MTX-treated (bottom) mice tumor tissues of MRT PDX models 103T (D) and 78T (E). Scale bars: 200 μm.

(F and G) Scatterplots showing Ki67 labeling index in saline vehicle-treated (blue) and MTX-treated (purple) tumor tissues derived from MRT PDX models 103T (F) and 78T (G). Individual data points as well as the mean ± SD are given. p value was calculated using a two-tailed Mann-Whitney U test (**, $p < 0.01$).

MRT growth.[69,70] In conjunction with our discoveries, these studies suggest a pivotal role of pyrimidines in MRT that could potentially serve as a therapeutic vulnerability for these markedly aggressive tumors.

In conclusion, we here demonstrate that mapping the metabolic landscape of patient-derived tumoroids can be used to identify tumor-specific metabolic traits that can be exploited therapeutically. By comparing the metabolome of normal kidney organoids and pediatric kidney tumoroids, we found *de novo* nucleotide synthesis to be an MRT-specific metabolic vulnerability that can be therapeutically exploited by MTX and BAY treatment *in vitro* and by MTX treatment *in vivo.* Our studies support future (pre-)clinical investigation of these compounds for the treatment of children with rhabdoid tumors, which can ultimately lead to better treatment options for the currently incurable MRT.

Limitations of the study

This study has several limitations. Our results show that, in the absence of BAY, nucleoside supplementation enhanced survival by 30% in one of the MRT models. These data suggest that MRT cells can take up and scavenge circulating nucleosides or nucleobases from their environment and rely less on *de novo* nucleotide synthesis when exogenous supply is available. Future *in vitro* experiments under conditions that more accurately reflect physiological nutrient concentrations,[71,72] such as human plasma-like serum,[73] Plasmax,[74] or tumor interstitial fluid-based media,[75] would further strengthen the robustness of our (tumor) organoid models and the validity of the proposed therapeutic strategy. In addition, assessment of nucleotide levels in tumor tissues and blood during treatment with nucleotide inhibitors could demonstrate more comprehensively that the observed delay in MRT growth *in vivo* is primarily attributable to reduced intratumoral nucleotide pools, rather than secondary or systemic effects of the drugs. Lastly, this study did not address the potential mechanisms of resistance and combination therapies, which may be warranted considering the aggressive nature of MRT.

RESOURCE AVAILABILITY

Lead contact

Further information and requests for resources and reagents should be directed to and will be fulfilled by the lead contact, Jarno Drost (j.drost@prinsesmaximacentrum.nl).

Materials availability

This study did not generate new unique reagents.

Data and code availability

- RNA sequencing data have been deposited to the European Genome-Phenome Archive (https://ega-archive.org/ega/) under accession numbers EGAD00001005319, EGAD00001005318, and EGAD00001015391
- The original data and code have been deposited at Zenodo (https://doi.org/10.5281/zenodo.14007800).
- Any additional information required to reanalyze the data reported in this work paper is available from the lead contact upon request, Jarno Drost (j.drost@prinsesmaximacentrum.nl).

ACKNOWLEDGMENTS

We are grateful to the patients and parents who agreed to participate in our research. We would like to thank the Preclinical Intervention Unit of the Mouse Clinic for Cancer and Aging (MCCA) at the NKI for performing the intervention studies and the Princess Máxima Center Biobank and Data Access Committee for providing tissues and data. C.R.B. and J.D. received funding from Foundation Children Cancer-free (KiKa #377), and J.D. from Oncode Accelerator, a Dutch National Growth Fund project under grant number NGFOP2201.

AUTHOR CONTRIBUTIONS

F.M.-R., C.R.B., and J.D. designed the study. F.M.-R., M.M.G.K., and E.A.Z. performed the experiments and data analyses. All co-authors were involved in data curation. T.d.S. supported bioinformatics analyses. N.P. and M.v.d.V. performed *in vivo* experiments. J.W.A.J. provided technical support during mass spectrometry experiments. M.M.G.K., E.A.Z., C.R.B., and J.D. wrote the manuscript, which was reviewed by all co-authors.

DECLARATION OF INTERESTS

The authors declare no competing interests.

STAR★METHODS

Detailed methods are provided in the online version of this paper and include the following:

- KEY RESOURCES TABLE
- EXPERIMENTAL MODEL AND STUDY PARTICIPANT DETAILS
  - Animals
  - Human tissue
  - Patient-derived organoids
- METHOD DETAILS
  - Bulk RNA sequencing
  - Drug screens
  - Flow cytometric analysis of Annexin V/DAPI positive cells
  - Folinic acid/nucleoside rescue after drug treatment
  - Liquid chromatography – Mass spectrometry (LC-MS)-based metabolomics
  - Histology and immunohistochemistry
  - *In vivo* studies
- QUANTIFICATION AND STATISTICAL ANALYSIS

SUPPLEMENTAL INFORMATION

Supplemental information can be found online at https://doi.org/10.1016/j.xcrm.2024.101878.

Received: November 22, 2023
Revised: August 27, 2024
Accepted: November 26, 2024
Published: December 20, 2024

REFERENCES

1. Van den Heuvel-Eibrink, M.M., van Tinteren, H., Rehorst, H., Coulombe, A., Patte, C., de Camargo, B., de Kraker, J., Leuschner, I., Lugtenberg, R., Pritchard-Jones, K., et al. (2011). Malignant rhabdoid tumours of the kidney (MRTKs), registered on recent SIOP protocols from 1993 to 2005: A report of the SIOP renal tumour study group. Pediatr. Blood Cancer *56*, 733–737. https://doi.org/10.1002/PBC.22922.
2. Parham, D.M., Weeks, D.A., and Beckwith, J.B. (1994). The clinicopathologic spectrum of putative extrarenal rhabdoid tumors. An analysis of 42 cases studied with immunohistochemistry or electron microscopy. Am. J. Surg. Pathol. *18*, 1010–1029. https://doi.org/10.1097/00000478-199410000-00005.
3. Rorke, L.B., Packer, R.J., and Biegel, J.A. (1996). Central nervous system atypical teratoid/rhabdoid tumors of infancy and childhood: definition of

an entity. J. Neurosurg. *85*, 56–65. https://doi.org/10.3171/JNS.1996.85.1.0056.

4. Louis, D.N., Perry, A., Reifenberger, G., von Deimling, A., Figarella-Branger, D., Cavenee, W.K., Ohgaki, H., Wiestler, O.D., Kleihues, P., and Ellison, D.W. (2016). The 2016 World Health Organization Classification of Tumors of the Central Nervous System: a summary. Acta Neuropathol. *131*, 803–820. https://doi.org/10.1007/S00401-016-1545-1.

5. Nemes, K., Johann, P.D., Steinbügl, M., Gruhle, M., Bens, S., Kachanov, D., Teleshova, M., Hauser, P., Simon, T., Tippelt, S., et al. (2022). Infants and Newborns with Atypical Teratoid Rhabdoid Tumors (ATRT) and Extracranial Malignant Rhabdoid Tumors (eMRT) in the EU-RHAB Registry: A Unique and Challenging Population. Cancers *14*, 2185. https://doi.org/10.3390/CANCERS14092185.

6. Torchia, J., Golbourn, B., Feng, S., Ho, K.C., Sin-Chan, P., Vasiljevic, A., Norman, J.D., Guilhamon, P., Garzia, L., Agamez, N.R., et al. (2016). Integrated (epi)-Genomic Analyses Identify Subgroup-Specific Therapeutic Targets in CNS Rhabdoid Tumors. Cancer Cell *30*, 891–908. https://doi.org/10.1016/J.CCELL.2016.11.003.

7. Ho, B., Johann, P.D., Grabovska, Y., De Dieu Andrianteranagna, M.J., Yao, F., Frühwald, M., Hasselblatt, M., Bourdeaut, F., Williamson, D., Huang, A., and Kool, M. (2020). Molecular subgrouping of atypical teratoid/rhabdoid tumors—a reinvestigation and current consensus. Neuro Oncol. *22*, 613–624. https://doi.org/10.1093/NEUONC/NOZ235.

8. Chun, H.J.E., Lim, E.L., Heravi-Moussavi, A., Saberi, S., Mungall, K.L., Bilenky, M., Carles, A., Tse, K., Shlafman, I., Zhu, K., et al. (2016). Genome-Wide Profiles of Extra-cranial Malignant Rhabdoid Tumors Reveal Heterogeneity and Dysregulated Developmental Pathways. Cancer Cell *29*, 394–406. https://doi.org/10.1016/J.CCELL.2016.02.009.

9. Gadd, S., Sredni, S.T., Huang, C.C., and Perlman, E.J.; Renal Tumor Committee of the Children's Oncology Group (2010). Rhabdoid tumor: Gene expression clues to pathogenesis and potential therapeutic targets. Lab. Invest. *90*, 724–738. https://doi.org/10.1038/LABINVEST.2010.66.

10. Young, M.D., Mitchell, T.J., Custers, L., Margaritis, T., Morales-Rodriguez, F., Kwakwa, K., Khabirova, E., Kildisiute, G., Oliver, T.R.W., de Krijger, R.R., et al. (2021). Single cell derived mRNA signals across human kidney tumors. Nat. Commun. *12*, 3896. https://doi.org/10.1038/s41467-021-23949-5.

11. Custers, L., Khabirova, E., Coorens, T.H.H., Oliver, T.R.W., Calandrini, C., Young, M.D., Vieira Braga, F.A., Ellis, P., Mamanova, L., Segers, H., et al. (2021). Somatic mutations and single-cell transcriptomes reveal the root of malignant rhabdoid tumours. Nat. Commun. *12*, 1407. https://doi.org/10.1038/s41467-021-21675-6.

12. Lee, R.S., Stewart, C., Carter, S.L., Ambrogio, L., Cibulskis, K., Sougnez, C., Lawrence, M.S., Auclair, D., Mora, J., Golub, T.R., et al. (2012). A remarkably simple genome underlies highly malignant pediatric rhabdoid cancers. J. Clin. Invest. *122*, 2983–2988. https://doi.org/10.1172/JCI64400.

13. Biegel, J., Zhou, J.Y., Rorke, L., Stenstrom, C., Wainwright, L., and Fogelgren, B. (1999). Germ-line and acquired mutations of INI1 in atypical teratoid and rhabdoid tumors. Cancer Res. *59*, 74–79.

14. Hasselblatt, M., Nagel, I., Oyen, F., Bartelheim, K., Russell, R.B., Schüller, U., Junckerstorff, R., Rosenblum, M., Alassiri, A.H., Rossi, S., et al. (2014). SMARCA4-mutated atypical teratoid/rhabdoid tumors are associated with inherited germline alterations and poor prognosis. Acta Neuropathol. *128*, 453–456. https://doi.org/10.1007/S00401-014-1323-X.

15. Hanahan, D., and Weinberg, R.A. (2011). Hallmarks of cancer: The next generation. Cell *144*, 646–674. https://doi.org/10.1016/j.cell.2011.02.013.

16. Garber, K. (2016). Cancer anabolic metabolism inhibitors move into clinic. Nat. Biotechnol. *34*, 794–795. https://doi.org/10.1038/NBT0816-794.

17. Galluzzi, L., Kepp, O., Vander Heiden, M.G., and Kroemer, G. (2013). Metabolic targets for cancer therapy. Nat. Rev. Drug Discov. *12*, 829–846. https://doi.org/10.1038/nrd4145.

18. Martinez-Outschoorn, U.E., Peiris-Pagés, M., Pestell, R.G., Sotgia, F., and Lisanti, M.P. (2016). Cancer metabolism: a therapeutic perspective. Nat. Rev. Clin. Oncol. *14*, 11–31. https://doi.org/10.1038/nrclinonc.2016.60.

19. Wettersten, H.I., Aboud, O.A., Lara, P.N., and Weiss, R.H. (2017). Metabolic reprogramming in clear cell renal cell carcinoma. Nat. Rev. Nephrol. *13*, 410–419. https://doi.org/10.1038/NRNEPH.2017.59.

20. Hakimi, A.A., Reznik, E., Lee, C.H., Creighton, C.J., Brannon, A.R., Luna, A., Aksoy, B.A., Liu, E.M., Shen, R., Lee, W., et al. (2016). An Integrated Metabolic Atlas of Clear Cell Renal Cell Carcinoma. Cancer Cell *29*, 104–116. https://doi.org/10.1016/J.CCELL.2015.12.004.

21. Zecchini, V., and Frezza, C. (2017). Metabolic synthetic lethality in cancer therapy. Biochim. Biophys. Acta. Bioenerg. *1858*, 723–731. https://doi.org/10.1016/J.BBABIO.2016.12.003.

22. Zhu, H., Wang, X., Lu, S., and Ou, K. (2023). Metabolic reprogramming of clear cell renal cell carcinoma. Front. Endocrinol. *14*, 1195500. https://doi.org/10.3389/FENDO.2023.1195500.

23. Padala, S.A., and Kallam, A. (2023). Clear Cell Renal Carcinoma (StatPearls).

24. Badoiu, S.C., Greabu, M., Miricescu, D., Stanescu-Spinu, I.I., Ilinca, R., Balan, D.G., Balcangiu-Stroescu, A.E., Mihai, D.A., Vacaroiu, I.A., Stefani, C., and Jinga, V. (2023). PI3K/AKT/mTOR Dysregulation and Reprogramming Metabolic Pathways in Renal Cancer: Crosstalk with the VHL/HIF Axis. Int. J. Mol. Sci. *24*, 8391. https://doi.org/10.3390/IJMS24098391.

25. Guo, H., German, P., Bai, S., Barnes, S., Guo, W., Qi, X., Lou, H., Liang, J., Jonasch, E., Mills, G.B., and Ding, Z. (2015). The PI3K/AKT Pathway and Renal Cell Carcinoma. Journal of Genetics and Genomics *42*, 343–353. https://doi.org/10.1016/J.JGG.2015.03.003.

26. Ersahin, T., Tuncbag, N., and Cetin-Atalay, R. (2015). The PI3K/AKT/mTOR interactive pathway. Mol. Biosyst. *11*, 1946–1954. https://doi.org/10.1039/C5MB00101C.

27. Aoki, M., and Fujishita, T. (2017). Oncogenic Roles of the PI3K/AKT/mTOR Axis. Curr. Top. Microbiol. Immunol. *407*, 153–189. https://doi.org/10.1007/82_2017_6.

28. Motzer, R.J., Jonasch, E., Agarwal, N., Alva, A., Baine, M., Beckermann, K., Carlo, M.I., Choueiri, T.K., Costello, B.A., Derweesh, I.H., et al. (2022). Kidney Cancer, Version 3.2022, NCCN Clinical Practice Guidelines in Oncology. J. Natl. Compr. Canc. Netw. *20*, 71–90. https://doi.org/10.6004/JNCCN.2022.0001.

29. Wang, S.Z., Poore, B., Alt, J., Price, A., Allen, S.J., Hanaford, A.R., Kaur, H., Orr, B.A., Slusher, B.S., Eberhart, C.G., et al. (2019). Unbiased metabolic profiling predicts sensitivity of high MYC-expressing atypical teratoid/rhabdoid tumors to glutamine inhibition with 6-diazo-5-oxo-L-norleucine. Clin. Cancer Res. *25*, 5925–5936. https://doi.org/10.1158/1078-0432.CCR-19-0189.

30. Sachs, N., and Clevers, H. (2014). Organoid cultures for the analysis of cancer phenotypes. Curr. Opin. Genet. Dev. *24*, 68–73. https://doi.org/10.1016/J.GDE.2013.11.012.

31. Drost, J., and Clevers, H. (2018). Organoids in cancer research. Nat. Rev. Cancer *18*, 407–418. https://doi.org/10.1038/s41568-018-0007-6.

32. Sato, T., Stange, D.E., Ferrante, M., Vries, R.G.J., Van Es, J.H., Van den Brink, S., Van Houdt, W.J., Pronk, A., Van Gorp, J., Siersema, P.D., and Clevers, H. (2011). Long-term expansion of epithelial organoids from human colon, adenoma, adenocarcinoma, and Barrett's epithelium. Gastroenterology *141*, 1762–1772. https://doi.org/10.1053/J.GASTRO.2011.07.050.

33. Gao, D., Vela, I., Sboner, A., Iaquinta, P.J., Karthaus, W.R., Gopalan, A., Dowling, C., Wanjala, J.N., Undvall, E.A., Arora, V.K., et al. (2014). Organoid cultures derived from patients with advanced prostate cancer. Cell *159*, 176–187. https://doi.org/10.1016/J.CELL.2014.08.016.

34. Boj, S.F., Hwang, C.I., Baker, L.A., Chio, I.I.C., Engle, D.D., Corbo, V., Jager, M., Ponz-Sarvise, M., Tiriac, H., Spector, M.S., et al. (2015). Organoid models of human and mouse ductal pancreatic cancer. Cell *160*, 324–338. https://doi.org/10.1016/J.CELL.2014.12.021.

35. Broutier, L., Mastrogiovanni, G., Verstegen, M.M., Francies, H.E., Gavarró, L.M., Bradshaw, C.R., Allen, G.E., Arnes-Benito, R., Sidorova, O., Gaspersz, M.P., et al. (2017). Human Primary Liver Cancer–Derived Organoid Cultures for Disease Modeling and Drug Screening. Nature *23*, 1424–1435. https://doi.org/10.1038/nm.4438.

36. Sachs, N., de Ligt, J., Kopper, O., Gogola, E., Bounova, G., Weeber, F., Balgobind, A.V., Wind, K., Gracanin, A., Begthel, H., et al. (2018). A Living Biobank of Breast Cancer Organoids Captures Disease Heterogeneity. Cell *172*, 373–386.e10. https://doi.org/10.1016/J.CELL.2017.11.010.

37. Schutgens, F., Rookmaaker, M.B., Margaritis, T., Rios, A., Ammerlaan, C., Jansen, J., Gijzen, L., Vormann, M., Vonk, A., Viveen, M., et al. (2019). Tubuloids derived from human adult kidney and urine for personalized disease modeling. Nat. Biotechnol. *37*, 303–313. https://doi.org/10.1038/s41587-019-0048-8.

38. Calandrini, C., Schutgens, F., Oka, R., Margaritis, T., Candelli, T., Mathijsen, L., Ammerlaan, C., van Ineveld, R.L., Derakhshan, S., de Haan, S., et al. (2020). An organoid biobank for childhood kidney cancers that captures disease and tissue heterogeneity. Nat. Commun. *11*, 1310. https://doi.org/10.1038/s41467-020-15155-6.

39. Calandrini, C., van Hooff, S.R., Paassen, I., Ayyildiz, D., Derakhshan, S., Dolman, M.E.M., Langenberg, K.P.S., van de Ven, M., de Heus, C., Liv, N., et al. (2021). Organoid-based drug screening reveals neddylation as therapeutic target for malignant rhabdoid tumors. Cell Rep. *36*, 109568. https://doi.org/10.1016/J.CELREP.2021.109568.

40. Meister, M.T., Groot Koerkamp, M.J.A., de Souza, T., Breunis, W.B., Frazer-Mendelewska, E., Brok, M., DeMartino, J., Manders, F., Calandrini, C., Kerstens, H.H.D., et al. (2022). Mesenchymal tumor organoid models recapitulate rhabdomyosarcoma subtypes. EMBO Mol. Med. *14*, e16001. https://doi.org/10.15252/EMMM.202216001.

41. Paassen, I., Williams, J., Ríos Arceo, C., Ringnalda, F., Mercer, K.S., Buhl, J.L., Moreno, N., Federico, A., Franke, N.E., Kranendonk, M., et al. (2023). Atypical teratoid/rhabdoid tumoroids reveal subgroup-specific drug vulnerabilities. Oncogene *42*, 1661–1671. https://doi.org/10.1038/s41388-023-02681-y.

42. Grossman, R.L., Heath, A.P., Ferretti, V., Varmus, H.E., Lowy, D.R., Kibbe, W.A., and Staudt, L.M. (2016). Toward a Shared Vision for Cancer Genomic Data. N. Engl. J. Med. *375*, 1109–1112. https://doi.org/10.1056/NEJMP1607591.

43. Abromowitch, M., Ochs, J., Pui, C.-H., Kalwinsky, D., Rivera, G.K., Fairclough, D., Look, A.T., Hustu, H.O., Murphy, S.B., and Evans, W.E. (1988). High-dose methotrexate improves clinical outcome in children with acute lymphoblastic leukemia: St. Jude total therapy study X. Med. Pediatr. Oncol. *16*, 297–303. https://doi.org/10.1002/MPO.2950160502.

44. Hutchins, L.F., Green, S.J., Ravdin, P.M., Lew, D., Martino, S., Abeloff, M., Lyss, A.P., Allred, C., Rivkin, S.E., and Osborne, C.K. (2005). Randomized, controlled trial of cyclophosphamide, methotrexate, and fluorouracil versus cyclophosphamide, doxorubicin, and fluorouracil with and without tamoxifen for high-risk, node-negative breast cancer: treatment results of Intergroup Protocol INT-0102. J. Clin. Oncol. *23*, 8313–8321. https://doi.org/10.1200/JCO.2005.08.071.

45. Yu, J., Du, H., Ye, X., Zhang, L., and Xiao, H. (2021). High-dose methotrexate-based regimens and post-remission consolidation for treatment of newly diagnosed primary CNS lymphoma: meta-analysis of clinical trials. Sci. Rep. *11*, 2125. https://doi.org/10.1038/s41598-020-80724-0.

46. Wippel, B., Gundle, K.R., Dang, T., Paxton, J., Bubalo, J., Stork, L., Fu, R., Ryan, C.W., and Davis, L.E. (2019). Safety and efficacy of high-dose methotrexate for osteosarcoma in adolescents compared with young adults. Cancer Med. *8*, 111–116. https://doi.org/10.1002/CAM4.1898.

47. Slavc, I., Chocholous, M., Leiss, U., Haberler, C., Peyrl, A., Azizi, A.A., Dieckmann, K., Woehrer, A., Peters, C., Widhalm, G., et al. (2014). Atypical teratoid rhabdoid tumor: improved long-term survival with an intensive multimodal therapy and delayed radiotherapy. The Medical University of Vienna Experience 1992-2012. Cancer Med. *3*, 91–100. https://doi.org/10.1002/CAM4.161.

48. Shi, D.D., Savani, M.R., Levitt, M.M., Wang, A.C., Endress, J.E., Bird, C.E., Buehler, J., Stopka, S.A., Regan, M.S., Lin, Y.F., et al. (2022). De novo pyrimidine synthesis is a targetable vulnerability in IDH mutant glioma. Cancer Cell *40*, 939–956.e16. https://doi.org/10.1016/j.ccell.2022.07.011.

49. Pal, S., Kaplan, J.P., Nguyen, H., Stopka, S.A., Savani, M.R., Regan, M.S., Nguyen, Q.D., Jones, K.L., Moreau, L.A., Peng, J., et al. (2022). A druggable addiction to de novo pyrimidine biosynthesis in diffuse midline glioma. Cancer Cell *40*, 957–972.e10. https://doi.org/10.1016/J.CCELL.2022.07.012.

50. Gwynne, W.D., Suk, Y., Custers, S., Mikolajewicz, N., Chan, J.K., Zador, Z., Chafe, S.C., Zhai, K., Escudero, L., Zhang, C., et al. (2022). Cancer-selective metabolic vulnerabilities in MYC-amplified medulloblastoma. Cancer Cell *40*, 1488–1502.e7. https://doi.org/10.1016/J.CCELL.2022.10.009.

51. Spina, R., Mills, I., Ahmad, F., Chen, C., Ames, H.M., Winkles, J.A., Woodworth, G.F., and Bar, E.E. (2022). DHODH inhibition impedes glioma stem cell proliferation, induces DNA damage, and prolongs survival in orthotopic glioblastoma xenografts. Oncogene *41*, 5361–5372. https://doi.org/10.1038/s41388-022-02517-1.

52. Maddocks, O.D.K., Athineos, D., Cheung, E.C., Lee, P., Zhang, T., van den Broek, N.J.F., Mackay, G.M., Labuschagne, C.F., Gay, D., Kruiswijk, F., et al. (2017). Modulating the therapeutic response of tumours to dietary serine and glycine starvation. Nature *544*, 372–376. https://doi.org/10.1038/nature22056.

53. Zaal, E.A., Wu, W., Jansen, G., Zweegman, S., Cloos, J., and Berkers, C.R. (2017). Bortezomib resistance in multiple myeloma is associated with increased serine synthesis. Cancer Metab. *5*, 7. https://doi.org/10.1186/s40170-017-0169-9.

54. Cline, A., and Jorizzo, J.L. (2017). Does daily folic acid supplementation reduce methotrexate efficacy? Dermatol. Online J. *23*, 6. https://doi.org/10.5070/d32311037244.

55. Brennan, B., Stiller, C., and Bourdeaut, F. (2013). Extracranial rhabdoid tumours: What we have learned so far and future directions. Lancet Oncol. *14*, e329–e336. https://doi.org/10.1016/S1470-2045(13)70088-3.

56. Lowis S, Nicolin G, Pizer B, Clifford S, Anderson J. Guidelines for management of Atypical Teratoid Rhabdoid Tumours, version 2.2 Guidelines for management of Atypical Teratoid Rhabdoid Tumours CCLG Neuro-oncology Special Interest Group. Published online 2011.

57. Farber, S., Diamond, L.K., Mercer, R.D., Sylvester, R.F., and Wolff, J.A. (1948). Temporary remissions in acute leukemia in children produced by folic acid antagonist, 4-aminopteroyl-glutamic acid. N. Engl. J. Med. *238*, 787–793. https://doi.org/10.1056/NEJM194806032382301.

58. Koźmiński, P., Halik, P.K., Chesori, R., and Gniazdowska, E. (2020). Overview of Dual-Acting Drug Methotrexate in Different Neurological Diseases, Autoimmune Pathologies and Cancers. Int. J. Mol. Sci. *21*, 3483. https://doi.org/10.3390/IJMS21103483.

59. Bernhardt, M.B., Brown, A.L., Grim, A.T., Scheurer, M.E., El-Mallawany, N.K., and Ozuah, N.W. (2022). Safety analysis of high-dose methotrexate in pediatric non-Hodgkin lymphomas. Pediatr. Blood Cancer *69*, e29940. https://doi.org/10.1002/PBC.29940.

60. Krailo, M., Ertel, I., Makley, J., Fryer, C.J., Baum, E., Weetman, R., Yunis, E., Barnes, L., Bleyer, W.A., and Hammond, G.D. (1987). A randomized study comparing high-dose methotrexate with moderate-dose methotrexate as components of adjuvant chemotherapy in childhood nonmetastatic osteosarcoma: A report from the childrens cancer study group. Med. Pediatr. Oncol. *15*, 69–77. https://doi.org/10.1002/MPO.2950150205.

61. Meyers, P.A., Schwartz, C.L., Krailo, M., Kleinerman, E.S., Betcher, D., Bernstein, M.L., Conrad, E., Ferguson, W., Gebhardt, M., Goorin, A.M., et al. (2005). Osteosarcoma: a randomized, prospective trial of the addition of ifosfamide and/or muramyl tripeptide to cisplatin, doxorubicin, and high-dose methotrexate. J. Clin. Oncol. *23*, 2004–2011. https://doi.org/10.1200/JCO.2005.06.031.

62. Bacci, G., Picci, P., Ferrari, S., Ruggieri, P., Casadei, R., Tienghi, A., Brach del Prever, A., Gherlinzoni, F., Mercuri, M., and Monti, C. (1993). Primary

chemotherapy and delayed surgery for nonmetastatic osteosarcoma of the extremities. Results in 164 patients preoperatively treated with high doses of methotrexate followed by cisplatin and doxorubicin. Cancer *72*, 3227–3238. https://doi.org/10.1002/1097-0142(19931201)72:11.

63. Pompe, R.S., Von Bueren, A.O., Mynarek, M., von Hoff, K., Friedrich, C., Kwiecien, R., Treulieb, W., Lindow, C., Deinlein, F., Fleischhack, G., et al. (2015). Intraventricular methotrexate as part of primary therapy for children with infant and/or metastatic medulloblastoma: Feasibility, acute toxicity and evidence for efficacy. Eur. J. Cancer *51*, 2634–2642. https://doi.org/10.1016/J.EJCA.2015.08.009.
64. Allen, J.C., Walker, R., and Rosen, G. (1988). Preradiation high-dose intravenous methotrexate with leucovorin rescue for untreated primary childhood brain tumors. J. Clin. Oncol. *6*, 649–653. https://doi.org/10.1200/JCO.1988.6.4.649.
65. Pollack, I.F., Agnihotri, S., and Broniscer, A. (2019). Childhood brain tumors: Current management, biological insights, and future directions. J. Neurosurg. Pediatr. *23*, 261–273. https://doi.org/10.3171/2018.10.PEDS18377.
66. Sandberg, D.I., Rytting, M., Zaky, W., Kerr, M., Ketonen, L., Kundu, U., Moore, B.D., Yang, G., Hou, P., Sitton, C., et al. (2015). Methotrexate administration directly into the fourth ventricle in children with malignant fourth ventricular brain tumors: a pilot clinical trial. J. Neuro Oncol. *125*, 133–141. https://doi.org/10.1007/S11060-015-1878-Y.
67. Park, M., Han, J.W., Hahn, S.M., Lee, J.A., Kim, J.Y., Shin, S.H., Kim, D.S., Yoon, H.I., Hong, K.T., Choi, J.Y., et al. (2021). Atypical Teratoid/Rhabdoid Tumor of the Central Nervous System in Children under the Age of 3 Years. Cancer Res. Treat. *53*, 378–388. https://doi.org/10.4143/CRT.2020.756.
68. Howard, S.C., McCormick, J., Pui, C.H., Buddington, R.K., and Harvey, R.D. (2016). Preventing and Managing Toxicities of High-Dose Methotrexate. Oncol. *21*, 1471–1482. https://doi.org/10.1634/THEONCOLOGIST.2015-0164.
69. Matsubara, K., Yamasaki, K., Tanimura, K., Hira, K., Okuhiro, Y., Ishii, Y., Nitani, C., Okada, K., Fujisaki, H., and Hara, J. (2021). Gemcitabine and Docetaxel for the Treatment of Relapsed and Refractory Malignant Rhabdoid Tumor of Kidney and Atypical Teratoid Rhabdoid Tumor. Gan To Kagaku Ryoho. *48*, 537–540. https://europepmc.org/article/med/33976041.
70. Metselaar, D.S., Meel, M.H., Goulding, J.R., du Chatinier, A., Rigamonti, L., Waranecki, P., Geisemeyer, N., de Gooijer, M.C., Breur, M., Koster, J., et al. (2024). Gemcitabine therapeutically disrupts essential SIRT1-mediated p53 repression in atypical teratoid/rhabdoid tumors. Cell Rep. Med. *5*, 101700. https://doi.org/10.1016/J.XCRM.2024.101700.
71. Hennequart, M., Labuschagne, C.F., Tajan, M., Pilley, S.E., Cheung, E.C., Legrave, N.M., Driscoll, P.C., and Vousden, K.H. (2021). The impact of physiological metabolite levels on serine uptake, synthesis and utilization in cancer cells. Nat. Commun. *12*, 6176. https://doi.org/10.1038/S41467-021-26395-5.
72. Kes, M.M.G., Berkers, C.R., and Drost, J. (2024). Bridging the gap: advancing cancer cell culture to reveal key metabolic targets. Front. Oncol. *14*, 1480613. https://doi.org/10.3389/FONC.2024.1480613.
73. Cantor, J.R., Abu-Remaileh, M., Kanarek, N., Freinkman, E., Gao, X., Louissaint, A., Jr., Lewis, C.A., and Sabatini, D.M. (2017). Physiologic Medium Rewires Cellular Metabolism and Reveals Uric Acid as an Endogenous Inhibitor of UMP Synthase. Cell *169*, 258–272.e17. https://doi.org/10.1016/j.cell.2017.03.023.
74. Voorde, J.V., Ackermann, T., Pfetzer, N., Sumpton, D., Mackay, G., Kalna, G., Nixon, C., Blyth, K., Gottlieb, E., Tardito, S., et al. (2019). Improving the metabolic fidelity of cancer models with a physiological cell culture medium. Sci. Adv. *5*, eaau7314. https://doi.org/10.1126/SCIADV.AAU7314.
75. Saab, J.J.A., Dzierozynski, L.N., Jonker, P.B., AminiTabrizi, R., Shah, H., Menjivar, R.E., Scott, A.J., Nwosu, Z.C., Zhu, Z., Chen, R.N., et al. (2023). Pancreatic tumors exhibit myeloid-driven amino acid stress and upregulate arginine biosynthesis. Elife *12*, e81289. https://doi.org/10.7554/ELIFE.81289.
76. Ruifrok, A., and Johnston, D.A. (2001). Quantification of histochemical staining by color deconvolution. Anal. Quant. Cytol. Histol. *23*, 291–299.

STAR★METHODS

KEY RESOURCES TABLE

REAGENT or RESOURCE	SOURCE	IDENTIFIER
Antibodies		
APC-Annexin V	BD Biosciences	Cat# 550475 RRID: AB_2868885
DAPI	ThermoFisher	Cat# D1306; RRID: AB_2629482
Ki67	Leica, BOND™	Cat# PA0118
Biological samples		
Patient-derived organoid line 60T (MRT)	Calandrini et al.[38]	DOI: https://doi.org/10.1038/s41467-020-15155-6
Patient-derived organoid line 78T (MRT)	Calandrini et al.[38]	DOI: https://doi.org/10.1038/s41467-020-15155-6
Patient-derived organoid line 103T (MRT)	Calandrini et al.[38]	DOI: https://doi.org/10.1038/s41467-020-15155-6
Patient-derived organoid line JD081T (MRT)	Calandrini et al.[38]	DOI: https://doi.org/10.1038/s41467-020-15155-6
Patient-derived organoid line 51T (Wilms)	Calandrini et al.[38]	DOI: https://doi.org/10.1038/s41467-020-15155-6
Patient-derived organoid line 68T (Wilms)	Calandrini et al.[38]	DOI: https://doi.org/10.1038/s41467-020-15155-6
Patient-derived organoid line 80T (Wilms)	Calandrini et al.[38]	DOI: https://doi.org/10.1038/s41467-020-15155-6
Patient-derived organoid line 86T (Wilms)	Calandrini et al.[38]	DOI: https://doi.org/10.1038/s41467-020-15155-6
Patient-derived organoid line 88T (Wilms)	Calandrini et al.[38]	DOI: https://doi.org/10.1038/s41467-020-15155-6
Patient-derived organoid line 119T (Rel. Wilms)	Calandrini et al.[38]	DOI: https://doi.org/10.1038/s41467-020-15155-6
Patient-derived organoid line 123T (Rel. Wilms)	Calandrini et al.[38]	DOI: https://doi.org/10.1038/s41467-020-15155-6
Patient-derived organoid line 125T (Rel. Wilms)	Calandrini et al.[38]	DOI: https://doi.org/10.1038/s41467-020-15155-6
Patient-derived organoid line 126T (Rel. Wilms)	Calandrini et al.[38]	DOI: https://doi.org/10.1038/s41467-020-15155-6
Patient-derived organoid line 16H (Normal)	Calandrini et al.[38]	DOI: https://doi.org/10.1038/s41467-020-15155-6
Patient-derived organoid line 57H (Normal)	Calandrini et al.[38]	DOI: https://doi.org/10.1038/s41467-020-15155-6
Patient-derived organoid line 60H (Normal)	Calandrini et al.[38]	DOI: https://doi.org/10.1038/s41467-020-15155-6
Patient-derived organoid line 71H (Normal)	Calandrini et al.[38]	DOI: https://doi.org/10.1038/s41467-020-15155-6
Patient-derived tumoroid line ATRT-04 (AT/RT-SHH)	Paassen et al.[41]	DOI: https://doi.org/10.1038/s41388-023-02681-y
Patient-derived tumoroid line ATRT-05 (AT/RT-SHH)	Paassen et al.[41]	DOI: https://doi.org/10.1038/s41388-023-02681-y
Patient-derived tumoroid line ATRT-18 (AT/RT-SHH)	Paassen et al.[41]	DOI: https://doi.org/10.1038/s41388-023-02681-y
Patient-derived tumoroid line ATRT-06 (AT/RT-MYC)	Paassen et al.[41]	DOI: https://doi.org/10.1038/s41388-023-02681-y
Patient-derived tumoroid line ATRT-07 (AT/RT-MYC)	Paassen et al.[41]	DOI: https://doi.org/10.1038/s41388-023-02681-y
Patient-derived tumoroid line ATRT-08 (AT/RT-MYC)	Paassen et al.[41]	DOI: https://doi.org/10.1038/s41388-023-02681-y
Patient-derived tumoroid line BM-MRT20 (MRT brain metastasis)	Paassen et al.[41]	DOI: https://doi.org/10.1038/s41388-023-02681-y
Chemicals, peptides, and recombinant proteins		
A83-01	Tocris	Cat# 2939/10
Acetonitrile ULC/MS grade	Biosolve	Cat# 012041
Advanced DMEM/F12	ThermoFisher Scientific	Cat# 12634010
B27 supplement	ThermoFisher Scientific	Cat# 17504044
BAY-2402234 (Orludodstat)	DC Chemicals	Cat# DC23745
BME	Cultrex	Cat# 3533-010-02
D-Glucose	Gibco	Cat# 15023-021
EGF	Peprotech	Cat# AF-100-15
EmbryoMax Nucleosides	Sigma-Aldrich	Cat# ES-008-D
FGF10	Peprotech	Cat# 100-26
Folinic Acid (Leucovorin)	Sigma-Aldrich	Cat# 47612

(*Continued on next page*)

Continued

REAGENT or RESOURCE	SOURCE	IDENTIFIER
GlutaMAX	Gibco	Cat# 35050061
HEPES	Gibco	Cat# 15630106
L-Glutamine	Gibco	Cat# 25030081
LC/MS grade water	Biosolve	Cat# 232178
Methanol ULC/MS grade	Biosolve	Cat# 136841
Methotrexate	Merck	Cat# M1000000
N-acetylcysteine	Sigma Aldrich	Cat# A9165
Penicillin/Streptomycin	Gibco	Cat# 15140163
Primocin	Invivogen	Cat# ant-pm-1
RhoKinase inhibitor Y-27632	Abmole Bioscience	Cat# M1817
SILAC advanced DMEM/F12 Flex Media	ThermoFisher Scientific	Cat# A2494301
TRIzol™ Reagent	Invitrogen	Cat# 15596026
TrypLE Express	ThermoFisher Scientific	Cat# 12605010
[U-$^{13}C_6$]-Glucose	Cambridge isotope laboratories (Buchem)	Cat# CLM-1396-PK
Critical commercial assays		
CellTiter-Glo 3D reagent	Promega	Cat# G9683
Deposited data		
Processed data and scripts supporting this manuscript	This paper	https://doi.org/10.5281/zenodo.14007800
RNA bulk sequencing pediatric kidney tumors	Calandrini et al.[38]	EGA, EGAD00001005319 and EGAD00001005318
RNA bulk sequencing DMSO, MTX and BAY-treated normal kidney organoids and MRT tumoroids	This paper	EGA, EGAD00001015391
Experimental models: Organisms/strains		
NOD-Scid IL2Rgnull mice	The Jackson Laboratory	JAX (2210)
Software and algorithms		
GraphPad Prism v.9.3.1	GraphPad software	https://www.graphpad.com/
GSEA	Broad institute	https://www.gsea-msigdb.org/gsea/index.jsp
ImageJ	NIH	https://imagej.nih.gov/ij/
Color_Deconvolution2 algorithm[71]	ImageJ plugin	https://blog.bham.ac.uk/intellimic/g-landini-software/colour-deconvolution-2/
FlowJo software V10	BD Biosciences	https://www.bdbiosciences.com/en-us/products/software/flowjo-v10-software
RStudio software v4.3.3	RStudio	https://www.r-project.org/
TraceFinder software	ThermoFisher Scientific	https://www.thermofisher.com/order/catalog/product/OPTON-31001

EXPERIMENTAL MODEL AND STUDY PARTICIPANT DETAILS

Animals

Mouse experiments were conducted in agreement with the Animal Welfare Committee of the Royal Netherlands Academy of Arts and Sciences, and the Netherlands Cancer Institute, the Netherlands. 8-week-old NOD-Scid IL2Rgnull mice (male and female) were used as acceptors for subcutaneous injections of MRT organoids. Mice were randomized into groups without blinding. Handling injections, tumor measurements and culling of the mice was performed by the animal technicians of Intervention Unit team at the Mouse Cancer Clinic of the Netherlands Cancer Institute. Daily welfare check was performed by the animal caretakers and technicians of the Mouse Cancer Clinic. Mice were kept under standard temperature and humidity conditions in individually ventilated cages (Innovive), with food and water provided *ad libitum*. All animal experiments were approved by the Animal Welfare Committee of the Netherlands Cancer Institute and performed in accordance with institutional, national, and European guidelines for animal research (AVD30100202011584 EGP 24.4.10633, 24.1.10951 and AVD30100202011584 EGP 24.1.11316).

Human tissue

Approval for use of human material was provided by the medical ethical committee of the Erasmus Medical Center (Rotterdam, the Netherlands) and the Princess Máxima Center for pediatric oncology (Utrecht, the Netherlands). Written informed consent was provided by all patients and/or parents/guardians. Approval for use of the subject's tissue samples within the context of this study has been granted by the Máxima biobank and data access committee (https://research.prinsesmaximacentrum.nl/en/core-facilities/biobank-clinical-research-committee) (biobank request nr. PMCLAB2018.005 and PMCLAB2018.006). All organoid models used in this study were previously established by Calandrini et al. (2020),[38] Meister et al. (2022),[40] and Paassen et al. (2023).[41] An overview of the clinical characteristics of the patients from which the models were derived can be found in Table S3.

Patient-derived organoids

Experiments with human material were approved by the medical ethical committee of the Erasmus Medical Center (Rotterdam, the Netherlands) and Princess Máxima Center for Pediatric Oncology (Utrecht, the Netherlands). Informed consent was obtained from the parents of all participants. Approval for use of the subject's tissue samples within the context of this study has been granted by the Máxima biobank and data access committee (https://research.prinsesmaximacentrum.nl/en/core-facilities/biobank-clinical-research-committee) (biobank request nr. PMCLAB2018.005 and PMCLAB2018.006). Patient-derived kidney organoid cultures have been established with protocols previously described by Calandrini et al., 2020.[38] Normal kidney and kidney tumor organoids were cultured in reduced growth factor BME (Cultrex, 3533-010-02) topped with kidney organoid medium (KOM). KOM consists of AdDF+++ (Advanced DMEM/F12 containing 1x GlutaMAX, 10mM HEPES, and antibiotics; Gibco), supplemented with 1.5% B27 supplement (Gibco), 10% R-spondin-conditioned medium, EGF (50 ng/mL, Peprotech), FGF-10 (100 ng/mL, Peprotech), N-acetylcysteine (1.25 mM, Sigma), Rho-kinase inhibitor Y-27632 (10 μM, AbMole), and A83-01 (5 μM, Tocris Bioscience).[37] KOM was changed every 3–4 days, and organoids were passaged every 1–3 weeks. Organoids were either passaged by mechanical dissociation (MRT organoids), or with TrypLE Express (Invitrogen, 1260510) with 10 μM Rho-kinase inhibitor Y-27632 (normal kidney organoids, Wilms tumor organoids, RCC organoids). After adding 5–10 mL AdDF+++ and centrifugation at 300 rcf, cells were re-seeded in BME and topped with KOM. Atypical teratoid/rhabdoid tumoroid and rhabdomyosarcoma tumoroid cultures were maintained as described by Paassen et al. 2023 and Meister et al. 2022.

METHOD DETAILS

Bulk RNA sequencing

Bulk RNA sequencing on organoids and matching patient tissue was performed as described by Calandrini et al., 2020.[38] For bulk RNA sequencing on normal kidney model 103H and MRT model 103T upon 24-h treatment with DMSO, Methotrexate (MTX) or BAY-2402234 (BAY), 2.500 single cells/μL were seeded in a 6 well suspension plate (Greiner CELLSTAR, cat-no. 657-185) using 300 μL BME droplets per well (75% BME; 25% cell suspension) topped up with 2.5 mL of kidney organoid medium (KOM). Three (103T) to six days (103H) after seeding, medium was removed and exchanged for medium containing DMSO (vehicle), 400 nM MTX (Merck, M1000000), or 50 nM BAY (DC Chemicals, DC23745). After 24 h, RNA was extracted from the organoids using Trizol reagent (Invitrogen), and quality was checked with Bioanalyzer2100 RNA Nano 6000 chips (Agilent, Cat. 5067-1511).

The NEBNext Ultra RNA Library Prep Kit (New England Biolabs) was used to prepare sequencing libraries. Paired-end sequencing was performed on the Illumina HiSeq or Illumina NovaSeq X Plus by Novogene (Germany).

Bulk mRNA sequencing kidney data originating from Wilms and Rhabdoid tumors were downloaded from the TARGET database (ocg.cancer.gov/programs/target/data-matrix) through access links provided by NCBI. Paired-end files from each sample were downloaded with SRA-toolkit with parameters that kept only biological reads that passed quality filters and with no tags. After quality control with fastqc, raw files were aligned against human genome hg38 using STAR (v.2.7.2) and read counts quantified with featureCounts (v. 1.6.7) using genome annotation from Gencode v. 37.

Raw count files from each sample were then merged into a single matrix and processed in R 4.2.1 using the R package DESEq2. Prior to any downstream analysis the count matrix was filtered to keep only genes with at least 5 read counts across all samples, normalized, and transformed into $\log_2$ scale.

For both datasets, Gene Ontology analysis was performed using the R package clusterProfiler using a 0.05 q-value cutoff; heatmaps were generated with pheatmap.

Drug screens

Drug screens on rhabdomyosarcoma (RMS) organoids and atypical teratoid/rhabdoid tumoroids were performed as described by Meister et al., 2022[40] and Paassen et al. 2023.[41] For the kidney organoids, 500 cells per well were plated in a 5% BME slurry with KOM in black 384 wells plates (Corning), using a volume of 40 μL per well. Plating of the cells was done with a Multi-drop Combi Reagent 8 Dispenser (Thermo Scientific).

Methotrexate (Merck, M1000000) and BAY-2402234 (DC Chemicals, DC23745) were added with a Tecan D300e Digital Dispenser. Final concentrations used for drug screenings with Methotrexate were: 0.1 nM, 1 nM, 10 nM, 100 nM, 1 μM and 10 μM, and final concentrations for BAY-2402234 were: 0.01 nM, 0.05 nM, 1 nM, 10 nM, 100 nM and 1 μM. Drug concentrations were normalized

by the Tecan D300e dispenser for DMSO content. Cells treated with DMSO served as negative controls. For each organoid model, three independent experiments were performed, using four technical replicates per experiment.

120 h after adding the drugs, ATP levels were assessed with CellTiter-Glo 3D reagent (Promega) according to the manufacturer's instructions on a BMG Labtech FLUOstar Omega microplate reader. Results were normalized to DMSO vehicle (100%). Survival data was analyzed and visualized in GraphPad Prism (version 9.3.1). IC_{50} values were calculated in RStudio, using the drc package (v.3.0-1).

Flow cytometric analysis of Annexin V/DAPI positive cells

For this experiment, a slightly adjusted version of the protocol from Calandrini et al., 2021[39] was used. Normal kidney (lines 16H, 57H, 60H, 71H) and MRT organoids (lines 60T, 78T, 103T) were passaged 1:2 and 1:4, respectively, and plated in 75% BME droplets topped with KOM. After three (MRT organoids) to six days (normal kidney organoids), cells were re-plated in 5% BME slurry with KOM and treated with either DMSO, 400 nM MTX (Merck, M1000000) or 50 nM BAY-2402234 (DC Chemicals, DC23745). After 120 h, organoids and supernatant were harvested and made into a single-cell suspension using TrypLE Express (ThermoFisher) with Rho-kinase inhibitor Y-27632 (AbMole). Staining of single cells was done with APC-Annexin V (BD Biosciences, #550475) and DAPI (ThermoFisher, #D1306) in Annexin V binding buffer supplemented with 2.5mM Ca^{2+}. For flow cytometric analysis of the cells, the Beckman Cytoflex LX was used. Data were subsequently analyzed with FlowJo Software (BD Biosciences, version 10). Apoptotic indices were calculated by normalizing the percentages to DMSO controls (set to 1). Live and apoptotic fractions were calculated by dividing the number of events in that gated population through the sum of all gated events (Live + Early Apoptotic + Late Apoptotic = 1).

Folinic acid/nucleoside rescue after drug treatment

Organoids were dissociated and made into a single-cell solution using mechanical disruption. Single cells were plated at a density of 2.000–2.500 cells/μL in 5 μL 75% BME droplets topped with KOM in a flat-bottom 96 wells plate (Greiner, 655-160). For each condition, cells were plated in quadruplicate. After 48 h (78T and 103T) to 72 h (60T), treatment with DMSO, 400 nM MTX (Merck, M1000000) or BAY-2402234 (DC Chemicals, DC23745) alone or in combination with either 1x EmbryoMax Nucleosides (Sigma-Aldrich, ES-008-D) or 10 μM Folinic acid (Leucovorin, Sigma-Aldrich, #47612) was started. In all the wells, medium was refreshed daily, due to the instability of the nucleosides in the medium. All treatments lasted for 120 h. At the day of the readout, all medium was removed and 45 μL of adDF+++ together with 50 μL of the CellTiter-Glo 3D solution (Promega) was added to each well. After 5min of shaking and 30 min at RT in the dark, 80 μL of each well was transferred into a black clear bottom 396-wells plate (Corning). Luminescence was measured with the FLUOstar Omega microplate reader (BMG Labtech) and data was analyzed with GraphPad Prism software (version 9.3.1). Results were normalized to DMSO-only treated cells (100%) for each separate organoid line.

Liquid chromatography – Mass spectrometry (LC-MS)-based metabolomics

Kidney organoids

Normal kidney (lines 37H, 57H, 71H, 117H) and kidney tumor organoids (Wilms lines: 88T, 51T; MRT lines: 60T, 78T, 103T) were made single cell as described in previous sections. For each condition, $0.5x10^6$ cells were plated in triplicate in 75% BME droplets in KOM. When cells had reached confluency, 6 or 24-h labeling with [U-$^{13}C_6$]-glucose (Cambridge Isotopes, CLM-1396-PK) was started. For the LC-MS-based metabolomics experiments with MTX and BAY-2402234 in MRT organoids, $0.2\text{-}0.25x10^6$ single cells were immediately after plating treated with either DMSO, 400 nM MTX (Merck, M1000000) or 5 nM BAY-2402234 (DC Chemicals, DC23745) for a duration of 120 h. 96 h after adding the drugs, 24-h labeling with [U-$^{13}C_6$]-glucose was started. For labeling, adDF+++ culture medium was replaced for glucose-free SILAC Advanced DMEM/F-12 (Gibco, A2494301) supplemented with 17 mM [U-$^{13}C_6$]-glucose (Cambridge Isotopes, CLM-1396-PK), 2 mM L-Glutamine (Gibco, 25030081), 10 mM HEPES (Gibco, 15630080), 0.7 mM L-Arginine (Sigma-Aldrich, A5131), 0.5 mM L-Lysine (Sigma-Aldrich, L5626), and antibiotics. Since BME compositions could change after extended culturing, BME containing no cells was plated in triplicate for each tumor type to correct for possible background effects. 6 or 24 h after labeling, the medium was removed and all wells were washed with 1 mL cold PBS, without disrupting the BME droplets. PBS was removed and 500 μL ice-cold MS lysis solvent (LS) composed of methanol/acetonitrile/Milli-Q (2:2:1) was added to each well. Plates were put on a plate Rocker at 4°C for 10min to induce lysis. After 10min, LS was removed from the wells and collected in 1.5 mL Eppendorf tubes that were then put in a Thermoshaker at 4°C for 15 min. Samples were cleared by centrifugation at 12.000 rcf for 15 min. Samples were frozen at −80°C until further use.

AT/RT tumoroids

AT/RT tumoroids and MRT organoids were made single cell by mechanical dissociation, plating $0.5x10^6$ single cells in triplicate per condition in tumor stem medium (TSM, formulation described by Paassen et al. 2023). The next day, 6- or 24-h labeling with [U-$^{13}C_6$]-glucose was started. For labeling, TSM culture medium was replaced for a 50:50 mix of DMEM/F12 without glucose, glutamine and HEPES (Biowest, L0091) and Neurobasal A without glucose and sodium pyruvate (Gibco, A2477501), supplemented with 21.25 mM [U-$^{13}C_6$]-glucose (Cambridge Isotopes, CLM-1396-PK), 2 mM L-Glutamine (Gibco, 25030081), 10 mM HEPES (Gibco, 15630080), 1x MEM non-essential amino acid solution (Gibco, 11140050), 1.5 mM sodium pyruvate (Gibco, 11360070), and the standard growth factors.[41] 6 or 24 h after labeling, the medium was removed, cells were washed with cold PBS and lysed in 75 μL ice-cold LS for 10 min in a 4°C Thermoshaker. After 10 min, samples were cleared by centrifugation at 12.000 rcf for 15 min and frozen at −80°C until further use.

LC-MS analyses of metabolites were performed on a Q Exactive HF mass spectrometer (Thermo Scientific) coupled to a Vanquish autosampler and pump (Thermo Scientific) or Exactive mass spectrometer (Thermo Scientific) coupled to a Dionex Ultimate 3000 autosampler and pump (Thermo Scientific). Sample injection volumes were always 5 μL. The MS operated in polarity-switching mode with spray voltages of −3.5 kV and 4.5 kV. Sheath gas, auxiliary gas, and sweep gas flow rates were 35, 10, and 1 units, respectively. Separation of metabolites was done using a Sequant ZIC-pHILIC column (2.1 × 150 mm, 5 μm; Merck) coupled to a ZIC-pHILIC guard column (2.1 × 20 mm, 5 μm; Merck), using elution buffers acetonitrile for A, and 20mM $(NH_4)_2CO_3$, 0.1% NH_4OH in LC/MS grade water (Biosolve) for B. Column temperature was 30°C. Flow rates were set at 100 μL/min for the Q Exactive and 150 μL/min for the Exactive and a gradient ran from 80%A to 20%A. Data was analyzed using LCquan or TraceFinder software (Thermo Scientific). Identification and quantification of metabolites was based on exact mass within 5 ppm and validated further by concordance with m/z, retention times and peak shape of reference standards of metabolites of interest that were included in the same run. Peak intensities were normalized based on total ion count and distributions of isotopes were corrected for natural abundance of ^{13}C. The fraction of ^{13}C-labelled metabolites was calculated by dividing the amount of ^{13}C-labeled metabolites ([M+≥01]) by the total metabolite pool (sum of labeled [M+≥01] and unlabeled [M+00] isotopologues) multiplied by 100. The $\log_2$ fold-change (log2FC) in ^{13}C-labelled fractions was calculated for MTX- and BAY-treated tumoroids relative to DMSO controls. For visualization, the log2FC values were constrained by binning, using a lower threshold of −5 and an upper threshold of 5.

Histology and immunohistochemistry

Tissues were fixed in 4% paraformaldehyde, dehydrated, and embedded in paraffin. Formalin fixed and paraffin embedded (FFPE) tissues were cut into 4 μm sections using the HM-355S microtome (Thermo Fisher Scientific). Hematoxylin and eosin (HE) staining experiments were performed using a Ventana automated tissue staining system (BenchMark Ultra, Roche). Immunostaining for Ki67 was performed on an automated Leica BOND-III system, using a Ready-To-Use primary antibody against Ki67 (BOND, MM1, #PA0118). Quantification of Ki67 immunohistochemical staining was performed in ImageJ FIJI software, using the built-in H DAB vector of the Color_Deconvolution2 plugin.[76] Following deconvolution, manual thresholding was applied to the DAB-only image to determine the percentage Ki67-positive area. For each treatment condition, two different tumor tissues were analyzed. Within each tissue sample, Ki67-labeling quantification was performed in three different regions representative of the entire tumor tissue.

In vivo studies

250.000 small size MRT organoids (78T and 103T) were harvested and implanted subcutaneously in the right flank of NOD-Scid IL2Rgnull mice, using a 1:1 BME:Cell suspension.

When tumor volumes reached 100–150 mm^3, mice were put on a folic acid depleted diet (SAFE, #U8958, Version 194). After one week on the diet, mice were randomly assigned to either the MTX or saline treatment groups. Depending on the treatment group, mice received daily intraperitoneal injections of 0.75 mg/kg MTX (Emthexate PF, TEVA Pharmachemie) or saline for a total of three (78T) to four (103T) weeks.

Tumor volumes were monitored two (78T) or three (103T) times a week via caliper measurements. Mice were sacrificed when reaching humane endpoint (losing >20% body weight or having a tumor >1500 mm^3). When mice reached a tumor volume exceeding 1500 mm^3 before the end of the treatment, this volume (>1500 mm^3) was reported and maintained for that mouse until the treatment period was completed. Tumors and organs were collected for further histological analyses.

QUANTIFICATION AND STATISTICAL ANALYSIS

For comparison of live and early/late apoptotic cell fractions between DMSO control and drug treated organoids, multiple paired Student's t tests were used. To compare the mean percentages of viability of MRT organoids in the different treatment groups of the nucleotide/folinic acid rescue studies a one-way ANOVA Bonferroni's multiple comparisons test was used. For mass spectrometry experiments, P-values were acquired using Student's t tests using the mean peak areas of the different organoid models. The effect of organoid type (normal kidney or MRT) on glucose incorporation over time was analyzed using a linear model with an interaction term of class and time. Significant interaction between class and time was defined as an improved model fit with interaction term of class and time over a model lacking this interaction. For comparison of tumor volumes between the MTX- and saline treatment arms in the *in vivo* experiment a two-tailed unpaired Student's t tests was used. To compare the Ki67 labeling indices of MTX- and saline treated tumor tissues a two-tailed Mann-Whitney U test was used. p values < 0.05 were considered significant. All statistical data can be found in the figure legends.